foundations

MDPI

Article

Frequency Response Characterization of Coupled Hodgkin-Huxley Neurons in Kuramoto-Inspired Oscillator Network

Sarbani Das [1], Saptarshi Das [2,*] and Koushik Maharatna [1]

[1] School of Electronics and Computer Science, University of Southampton, Highfield Campus, University Road, Southampton SO17 1BJ, UK; sarbani.das@soton.ac.uk (S.D.); km3@ecs.soton.ac.uk (K.M.)
[2] Centre for Environmental Mathematics, Faculty of Environment, Science and Economy, University of Exeter, Penryn Campus, Penryn TR10 9FE, UK
* Correspondence: saptarshi.das@ieee.org

Abstract

Synchronization in networks of conductance-based neurons depends on the external stimulus, coupling architecture, coupling strength, and initial state of the constituent cells. In this work, we numerically investigate a finite all-to-all network of identical Hodgkin–Huxley (HH) neurons coupled through a normalized diffusive membrane-voltage term. The purpose is not to introduce a new neuronal model but to provide a joint finite-time characterization of the membrane voltage and the three ionic gating variables during the development of collective activity. Synchronization is quantified from pairwise state differences using matrix norms, whereas the short-time Fourier transform (STFT) and continuous wavelet transform (CWT) representations are used to describe the time-localized spectral content of the simulated trajectories. For the investigated parameter values and initial conditions, the coupled network exhibits convergence toward a common resting state, a transient single-spike response, sustained oscillatory responses, and transient intervals of reduced coherence followed by more coordinated firing. Increasing the applied current changes the observed response regime and dominant spectral component. Within the finite simulation windows considered here, the frequency estimates obtained from both time–frequency methods also show a small decreasing trend with an increase in coupling strength. This trend is reported as a numerical observation rather than as a universal asymptotic property because its magnitude may depend on the observation window, initial conditions, network size, and frequency-estimation procedure. The results illustrate how voltage coupling affects both the convergence of neuronal trajectories and the finite-time spectral characteristics of the membrane and gating-variable responses.

Keywords: Hodgkin–Huxley model; diffusively coupled neurons; synchronization error; transient dynamics; time–frequency analysis; continuous wavelet transform

Check for updates

Academic Editor: António M. Lopes

Received: 10 August 2026
Revised: 5 September 2026
Accepted: 29 September 2026
Published: 3 October 2026

Copyright: © 2026 by the authors. Licensee MDPI, Basel, Switzerland. This article is an open access article distributed under the terms and conditions of the Creative Commons Attribution (CC BY) license.

1. Introduction

Temporally coordinated activity among neuronal populations is an important feature of neural information processing [1–3]. Depending on the spatial scale, cellular properties, coupling mechanism, and physiological context, synchronization may support coherent communication among neuronal populations [4], whereas abnormal population coordination has been associated with several neurological and neuropsychiatric conditions [5–11].

These observations motivate mathematical studies of how collective neuronal activity depends on externally applied stimuli and interactions among cells. However, the present model should be interpreted as an idealized dynamical system rather than as a direct representation of a specific disease or of whole-brain anatomy.

The present work addresses a restricted question: how do identical conductance-based neurons evolve from different initial membrane states when they are connected through normalized all-to-all voltage coupling? Functional neural interactions in biological systems depend on task, anatomical organization, and pathological state [4,12,13]. In contrast, the homogeneous network considered here is used as a controlled numerical benchmark in which the effects of applied current, coupling strength, and ionic gating dynamics can be examined without introducing additional heterogeneity, noise, or sparse topology.

A range of neuronal models is available for studying collective dynamics. Phenomenological and reduced models, including integrate-and-fire, FitzHugh–Nagumo, and Morris–Lecar formulations, are particularly useful when analytical tractability or large network size is required [14–17]. Conductance-based models instead retain an explicit representation of membrane currents and ionic gating variables. These model classes should not be viewed as a simple hierarchy in which every reduced or extended model is merely a simplification of the classical HH system. For example, some conductance-based extensions include additional slow currents and can display bursting or adaptation not present in the original HH equations [18]. We use the classical HH model [19] as a canonical and reproducible four-state conductance-based system, not because it is universally the most realistic neuron model but because its membrane and gating variables permit a transparent joint state-space and frequency-domain analysis.

Synchronization has been studied in reduced and conductance-based neuronal networks under electrical coupling, transmission delay, noise, and phase reduction conditions and in different network architectures [20–28]. Other studies have addressed dynamic range, stochastic resonance, perturbation-induced desynchronization, and population-level descriptions of neuronal networks [29–32]. These contributions establish that numerical integration of coupled HH equations, phase portraits, or time–frequency transforms is not by itself a new methodology. Accordingly, the contribution of the present paper is framed more narrowly as a combined finite-time characterization of all four HH state variables, their pairwise synchronization errors, and their time-localized spectral content under a common all-to-all coupling protocol.

The network studied below uses direct membrane-voltage differences rather than the sinusoidal phase interaction of the classical Kuramoto equation. We therefore refer to it as a Kuramoto-inspired all-to-all topology or, more precisely, an all-to-all voltage-diffusively coupled HH network. Phase-reduction methods provide an established route from conductance-based oscillators to phase models in the weak-coupling regime [20,21,23]; such a reduction is not carried out here. The full four-state HH equations are retained so that membrane voltage, sodium activation, sodium inactivation, and potassium activation can be considered simultaneously.

Three complementary descriptions are used. First, time series and projected phase-space trajectories show how the simulated cells evolve from dispersed initial conditions. Second, pairwise state-difference matrices and their Frobenius and Euclidean norms quantify finite-time convergence among the cells, following the general use of synchronization errors in coupled nonlinear systems [33]. Third, the STFT and CWT representations describe how the spectral content of the simulated trajectories is distributed in time. These tools answer different questions: the error norms quantify similarity among cells, whereas the STFT and CWT characterize frequency content and are not independent synchronization measures.

The specific question addressed in this work is therefore not whether coupled Hodgkin–Huxley (HH) neurons can synchronize, which has been established in previous studies, but how the membrane voltage and all three ionic gating variables jointly evolve in state space, synchronization-error space, and time–frequency space when the applied current and normalized all-to-all diffusive voltage coupling are varied. Accordingly, the objective of this study is to provide a combined finite-time characterization of the evolution, convergence, and dominant spectral content of the four HH state variables within the same coupled network. The contribution should therefore be viewed as a numerical characterization of the coupled dynamics rather than as the proposal of a new neuronal model or synchronization theory.

The remainder of the paper is organized as follows. Section 2 defines the all-to-all voltage-coupled HH model, the synchronization-error measures, the time–frequency representations, and the numerical protocol. Section 3 describes the finite-time responses observed for selected values of the applied current and relates them to Figures 1–16. Section 4 examines the effect of coupling strength using Figures 17–25. Section 5 discusses interpretation and limitations, and Section 6 summarizes the conclusions supported by the investigated parameter range and simulation protocol.

2. Materials and Methods

2.1. The Mathematical Model

The HH model [19] is a 4-dimensional ODE, describing membrane potential V, activation of the Sodium Na+ gate m and Potassium K+ gate n, and inactivation of the Na+ gate h, as shown below:

$$\frac{dV}{dt} = \frac{1}{C_M}\Big(I - \overline{g}_{\mathrm{Na}} m^3 h (V - V_{\mathrm{Na}}) - \overline{g}_{\mathrm{K}} n^4 (V - V_{\mathrm{K}}) - \overline{g}_{\mathrm{L}} (V - V_{\mathrm{L}})\Big), \tag{1}$$

$$\frac{dm}{dt} = \alpha_m(1 - m) - \beta_m m, \tag{2}$$

$$\frac{dh}{dt} = \alpha_h(1 - h) - \beta_h h, \tag{3}$$

$$\frac{dn}{dt} = \alpha_n(1 - n) - \beta_n n. \tag{4}$$

Here, V is the membrane potential, C_M is the membrane capacitance per unit area, and I is the externally applied current density. The parameters $\bar{g}_{\mathrm{Na}}$, $\bar{g}_{\mathrm{K}}$, and $\bar{g}_L$ denote the maximum sodium, potassium, and leak conductances per unit area, respectively, whereas V_{Na}, V_{K}, and V_L are the corresponding reversal potentials. The variables m, h, and n represent Na^+ activation, Na^+ inactivation, and K^+ activation, respectively. The voltage-dependent functions $\alpha_x(V)$ and $\beta_x(V)$, where $x \in \{m, h, n\}$ describe the transition rates of the corresponding gating variables. The parameter values used here correspond to the classical squid-axon Hodgkin–Huxley formulation at 6.3 °C [19]:

$$V_{\mathrm{Na}} = 50\,\mathrm{mV}, \quad V_{\mathrm{K}} = -77\,\mathrm{mV}, \quad V_{\mathrm{L}} = -54.4\,\mathrm{mV},$$

$$\overline{g}_{\mathrm{Na}} = 120\,\mathrm{mS/cm^2}, \quad \overline{g}_{\mathrm{K}} = 36\,\mathrm{mS/cm^2}, \quad \overline{g}_{\mathrm{L}} = 0.3\,\mathrm{mS/cm^2}, \quad C_M = 1\,\mu\mathrm{F/cm^2},$$

$$\alpha_m(V) = \frac{0.1(V + 40)}{1 - \exp^{-(V+40)/10}}, \quad \beta_m(V) = 4\exp(-(V + 65)/18),$$

$$\alpha_h(V) = 0.07\exp(-(V + 65)/20), \quad \beta_h(V) = \frac{1}{1 + \exp(-(V + 35)/10)},$$

$$\alpha_n(V) = \frac{0.01(V + 55)}{1 - \exp(-(V + 55)/10)}, \quad \beta_n(V) = 0.125\exp(-(V + 65)/80).$$

The voltage-dependent rate functions $\alpha_x(V)$ and $\beta_x(V)$, $x \in \{m, h, n\}$ describe transitions of the corresponding gating variables between permissive and non-permissive states [19]. They should therefore be interpreted as channel-gating transition rates rather than as direct rates of ionic transfer across the membrane. The variable m represents Na^+ activation, h represents Na^+ inactivation, and n represents K^+ activation.

In order to model the diffusive transmembrane voltage coupling between each oscillator and all other oscillators, we modify Equation (1) by appending a linear voltage-coupling term $\frac{k}{N}\sum_{j=1}^{N}(V_j - V_i)$ where N is the number of neurons and k is the coupling parameter:

$$\begin{aligned} \frac{dV_i}{dt} &= \frac{1}{C_M}(I - \bar{g}_{\mathrm{Na}} m_i^3 h_i (V_i - V_{\mathrm{Na}}) - \bar{g}_{\mathrm{K}} n_i^4 (V_i - V_{\mathrm{K}}) - \bar{g}_{\mathrm{L}}(V_i - V_{\mathrm{L}})) + \frac{k}{N}\sum_{j=1}^{N}(V_j - V_i), \\ \frac{dm_i}{dt} &= \alpha_m(1 - m_i) - \beta_m m_i, \\ \frac{dh_i}{dt} &= \alpha_h(1 - h_i) - \beta_h h_i, \\ \frac{dn_i}{dt} &= \alpha_n(1 - n_i) - \beta_n n_i. \end{aligned} \tag{5}$$

The coupling term in Equation (5) can equivalently be expressed as:

$$\frac{k}{N}\sum_{j=1}^{N}(V_j - V_i) = k(\bar{V} - V_i), \qquad \bar{V} = \frac{1}{N}\sum_{j=1}^{N} V_j.$$

Thus, the diffusive coupling tends to reduce the instantaneous difference between the membrane potential of each neuron and the population-mean membrane potential. When complete voltage synchronization is reached, i.e., $V_1 = \cdots = V_N$, the coupling term becomes zero. This observation is useful for interpreting the synchronization and coupling-strength results presented below.

In order to compute the degree of synchrony of coupled HH cells, we calculated the synchronization error matrix of coupled oscillators at each time stamp. Then we calculated the Frobenius-norm and L_2 norm of state variables of each synchronization error matrix.

For each state variable $x \in \{V, m, h, n\}$, the pairwise synchronization error between neurons i and j is defined as $E_{ij}^x(t) = x_i(t) - x_j(t)$. The corresponding pairwise synchronization-error matrix is $E^x(t) = \left[E_{ij}^x(t)\right]_{i,j=1}^{N}$. Moreover,

$$\|E^x(t)\|_F = \sqrt{\sum_{i=1}^{N}\sum_{j=1}^{N}\left|E_{ij}^x(t)\right|^2}, \tag{6}$$

and

$$e_i^x(t) = \sqrt{\sum_{j=1}^{N}\left|x_i(t) - x_j(t)\right|^2}. \tag{7}$$

These quantities are used here as finite-time measures of convergence among the simulated state trajectories. A reduction in the synchronization error indicates that the corresponding states of the coupled neurons are approaching one another over the investigated simulation interval. Therefore, decay of these error measures is interpreted as numerical evidence of finite-time synchronization rather than as a formal proof of global asymptotic stability [33]. Since the norms are evaluated for a finite network and a finite observation time, their decay should be interpreted as numerical evidence of convergence within the investigated simulation window rather than as a formal proof of global asymptotic stability.

In order to compute sinusoidal frequency and phase content on local sections of the time series we divided the longer signals into shorter segments of equal length and then computed the Fourier transform separately on each shorter segment using the expression.

The short-time Fourier transform (STFT) of a signal $x(t)$ is defined as:

$$X(\tau, f) = \int_{-\infty}^{\infty} x(t)\, w(t-\tau)\, e^{-j2\pi f t}\, dt, \tag{8}$$

where $w(t)$ denotes the analysis window, τ is the center time of the window, and f denotes frequency. In the numerical implementation, the corresponding discrete form was evaluated for the sampled HH state-variable signals.

Thus it gives an estimate of the short-time, time-localized frequency content of the time series on shorter segments. We plotted the changing spectra as a function of time to generate the spectrogram of the time-varying frequency response.

In order to represent the signal as a weighted sum of shifted and scaled versions of a characteristic wave-like function we performed a CWT on the time series. The continuous wavelet transform (CWT) of a signal $x(t)$ is defined as:

$$W_x(a,b) = \frac{1}{\sqrt{|a|}} \int_{-\infty}^{\infty} x(t) \psi^* \left(\frac{t-b}{a} \right) dt, \tag{9}$$

where $a > 0$ denotes the scale, b is the translation parameter, $\psi(t)$ is the mother wavelet, and * denotes complex conjugation [34]. An analytic Morse wavelet is used for the CWT analysis in this study. The main purpose of the mother wavelet is to provide a source function to generate the daughter wavelets, which are simply the translated and scaled versions of the mother wavelet.

In order to calculate the dominant firing frequency we determined the frequency and time of the center of energy of each power spectrum estimate and chose the maximum power spectrum among all the windows in case of the STFT. In order to calculate the dominant firing frequency from the CWT response we determined the frequency of the maximum CWT coefficient of all the scales.

2.2. Numerical Implementation

In this section, we describe the numerical solution of N coupled differential equations of HH models and their time–frequency responses. We initially set the HH neurons in unsynchronized states by setting their initial membrane voltages based on uniformly distributed random numbers. Then, we used the iterative fourth-order Runge–Kutta (RK4) method to solve N nonlinear differential equations of the coupled HH model in a single time instance. To solve the equation, we simulated a 0.4 ms time-step size for the duration of 50–100 ms based on different scenarios. With specified initial conditions in each step, the RK4 approximation of the next value is determined by the previous value, apart from the first step, where the initial conditions are used, plus the weighted averages of four different increments, where each increment is the product of the step size and an estimated slope specified by function on the right-hand side of the differential equation.

Unless otherwise stated, the numerical analysis in Section 3 considers a finite all-to-all network of $N = 25$ identical HH neurons. The initial membrane voltages are selected from a uniform distribution over the interval $[-60,\ 0]$ mV, after which the model evolves deterministically according to the coupled HH equations. The differential equations are solved using the fourth-order Runge–Kutta (RK4) method. The applied-current and coupling-strength values used in the individual numerical experiments are reported in the corresponding sections and figure captions. The selected simulation duration is intended to characterize the transient and recurrent responses visible within a common finite-time window. Consequently, the phase portraits and synchronization errors presented below characterize the numerically observed trajectories over this interval. They are not used as a substitute for an analytical asymptotic-stability or bifurcation analysis.

To investigate the influence of parameter variation, the coupled HH system was simulated for selected values of the applied current and coupling strength [35]. The resulting responses are described using time series, projected phase portraits, synchronization-error measures, raster plots, and time–frequency representations. The phase portraits are interpreted as finite-time state-space trajectories associated with the simulated responses. No analytical stability or numerical bifurcation analysis was performed in the present study; consequently, the plotted trajectories are not used as a formal proof of asymptotic stability or attraction. It is to be noted that in our model only some of the initial states were considered as random variables to study the synchronization properties of the coupled oscillator network. Therefore, our work is fundamentally different from the other contemporary studies where additive Gaussian noise was considered on similar HH cells in one [25] or many state variables [26] to study noise-induced synchronization. Our model is deterministic in nature, with random initial conditions for which the effect of coupling strength and input current have been investigated on the dominant firing frequency using time–frequency analysis, phase portraits, norms of the synchronization error and raster plots [36–38].

To quantify synchronization among the coupled oscillators, we calculated the pairwise synchronization-error matrix defined above for each state variable. We performed a time–frequency analysis of the output signal by using the STFT and obtained the corresponding spectrogram. A spectrogram is a visual representation of the STFT. We divided each time series of membrane voltage and gating variables into small sections of window length N_w of 550 samples with a Hamming window. We specified an overlap of 549 samples between adjacent sections and evaluated the spectrum at [512/2 + 1]= 257 frequency rows and 512 [$\max(256, 2^p)$ where $p = \lceil \log_2 N_w \rceil$] DFT points. Then we applied a local Fourier transform on each section and obtained their frequency responses. Thus we got a number of frequency components. All of these frequency components at each section were plotted together to generate the frequency response output. Finally, we obtained a 2D visual heat map where the horizontal axis represents the temporal information of the signal, and the vertical axis represents the frequency axis.

In the STFT, the window size is set empirically and requires much experimentation. A larger window size gives better frequency resolution. Similarly, the smaller the window size, the better the localization in time but poorer the frequency decomposition. Because there is no optimal size with regard to window size that can give the best frequency response, wavelets are preferred when it comes to time–frequency domain decomposition. For each window, the segments are decomposed into smaller sections of dynamic width so a mixture of time and frequency domain localization can be obtained. Another reason for performing a wavelet transform is that the STFT gives better time–frequency analysis when the signal has a sinusoidal waveform. As the HH system is a nonlinear oscillator in nature, the phase portraits of state variables show non-sinusoidal periodic orbits. This led us to perform another time–frequency analysis of the signal using the CWT to generate the frequency output of the neural signals. Here, we used an analytic Morse wavelet to generate output from the CWT [39]. The plot of CWT coefficients for the signal is a 3D plot. The x-axis corresponds to the time shift. The y-axis represents frequency. The amplitude of the CWT coefficients is represented by the z-axis. Here, we used one neural signal in the frequency response plot as the average signal loses information in the transient phase. Our objective was to obtain the dominant frequency of the oscillations and then analyze how it is affected by the intrinsic parameters of the system. We used the highest value of the CWT coefficients to determine the dominant frequency components of the neural signal emitted after synchronization of the coupled cells. In the case of the STFT, the power spectral density (PSD) of the signal was also used for calculating the dominant frequency.

3. Frequency Response Analysis of Coupled HH Cells for Variation in Input Current

There have been numerous studies on the behavior of an ensemble of uncoupled HH cells for various input currents. In this section, we focus on the study of an ensemble of coupled HH cells with respect to various input currents. In our model, the coupling of HH cells is affected by their trans-membrane coupling voltage. In order to study the synchronization of coupled HH cells for various input currents the initial values of the resting membrane potentials of the HH cells were set with uniformly distributed random numbers so that initially the HH cells are not synchronized. We took the model of $N = 25$ HH cells coupled by coupling parameter k.

The current values considered in the following subsections were selected as representative operating points that produce qualitatively different finite-time responses. They were not obtained from a systematic bifurcation analysis and should therefore not be interpreted as precise boundaries between dynamical regimes. In particular, the interval between $I = 0.01$ and 1.5 $\mu A\,cm^{-2}$ was not exhaustively sampled.

3.1. Inactive Regime

When neurons do not fire any action potential for low-amplitude input current, it is called an inactive regime [14]. Here, we investigated the coupled HH cell model for a low-amplitude input current, I = 0.01 μAcm^{-2}. Figure 1 shows the temporal dynamics and frequency behavior of the membrane potential and ion channel gates for the given input current. As shown in Figure 1a–d the time series of the membrane potential, Na+ activation gate, K+ activation gate and Na+ inactivation gate of the coupled HH cells are not synchronized initially, then gradually they are synchronized and later reach a stable resting potential. The frequency response of the STFT of membrane voltage and dynamics of the Na+ activation gate, K+ activation gate and Na+ inactivation gate is shown in Figure 1e, Figure 1f, Figure 1g, and Figure 1h respectively, where one can see the frequencies that have maximum strength marked by a red hue, and the frequency of least power is denoted by a blue hue. As the system has reached the resting state, the frequency strength also shows very low (marked by a blue hue) in the spectrogram. The frequency response of the CWT for membrane voltage, Na+ activation gate, K+ activation gate and Na+ inactivation gate is shown in Figure 1i–l respectively. The scalogram image of the CWT shows the transient activity oscillations of different frequency components. The reddish hue shows that high-frequency activity occurs only at the beginning after that system has no oscillation. Figure 2 shows the evolution path of state variables of the membrane voltage V, Na+ activation gate m, Na+ inactivation gate h and K+ activation gate n via phase portraits. The stable fixed point in the phase portraits where system evolution trajectory is spiraling down denotes the equilibrium state of the system. Also, the open non-cyclic trajectories in the phase portraits confirm that the system does not enter any periodic firing state for the given parameter set; rather, it goes to a stable equilibrium state. The time evolution of the synchronization performance of coupled oscillators in the inactive regime shown in Figure 3 shows that with time, the synchronization error in both the Frobenius norm and L_2 norm plots decreases below the order of 10^{-10} on the logarithmic scale.

The spiral-like trajectories in Figure 2 represent the finite-time approach from the selected initial conditions toward the terminal region associated with the resting response. The open, non-recurrent trajectories are therefore consistent with relaxation toward an equilibrium rather than sustained periodic firing. This interpretation is independently supported by Figure 3, where both synchronization-error measures decrease to very small values over the simulated interval.

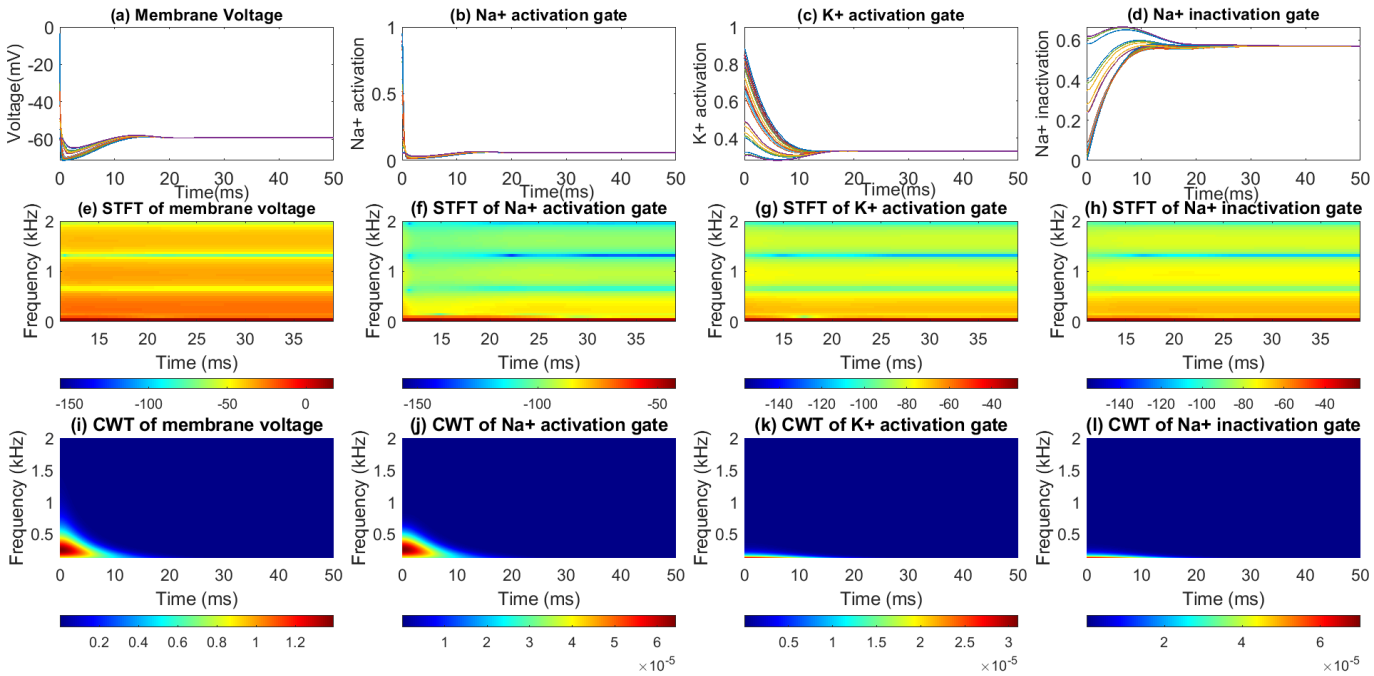


Figure 1. For input current $I = 0.01$ μAcm^{-2}: (**a**) membrane voltage vs. time; (**b**) Na+ activation gate vs. time; (**c**) K+ activation gate vs. time; (**d**) Na+ inactivation gate vs. time; (**e**) STFT of membrane voltage; (**f**) STFT of Na+ activation gate; (**g**) STFT of K+ activation gate; (**h**) STFT of Na+ inactivation gate; (**i**) CWT of membrane voltage; (**j**) CWT of Na+ activation gate; (**k**) CWT of K+ activation gate; (**l**) CWT of Na+ inactivation gate.

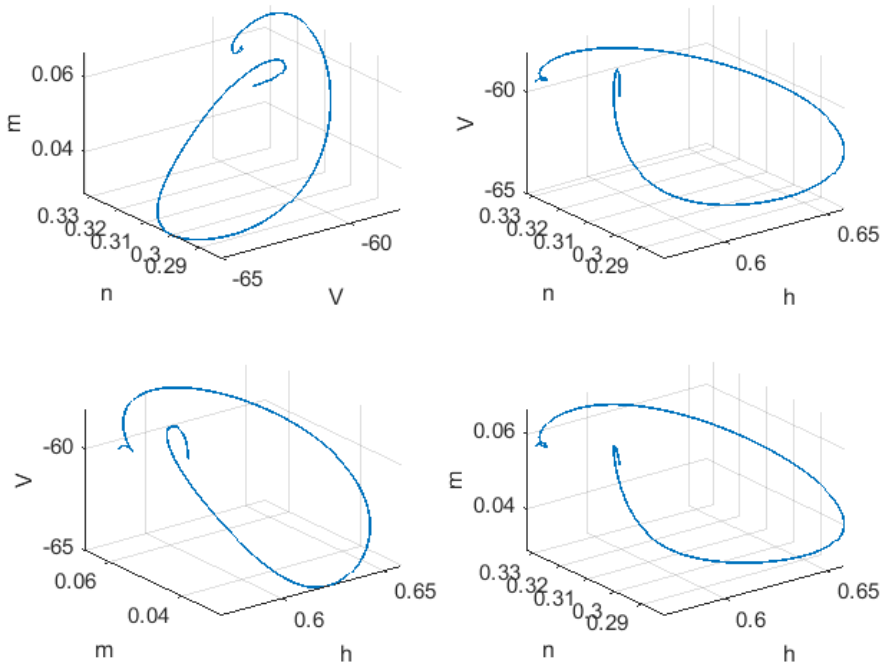


Figure 2. Phase portraits of neural signal when input current $I = 0.01$ μAcm^{-2}; M—membrane voltage; m—Na+ activation gate; h—Na+ inactivation gate; n—K+ activation gate.

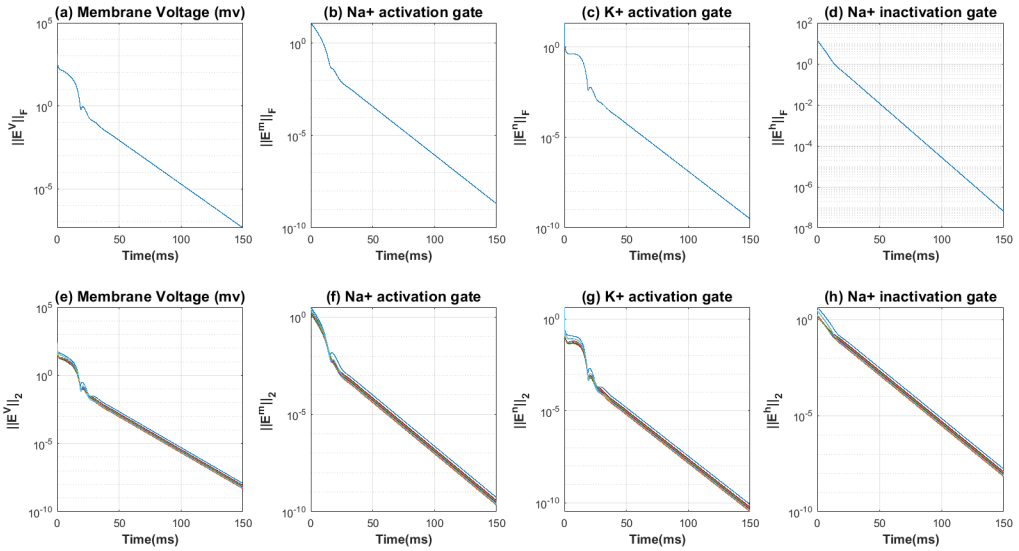


Figure 3. Synchronization error in Frobenius norm and L_2 norm logarithmic scales for input current $I = 0.01$ μAcm^{-2}.

3.2. Single-Spike Regime

Here, we explored coupled HH cell models for a low value of input current, which leads the HH system to fire a single spike and then return to a steady-state. Figure 4a shows that, for stimulus input current $I = 0.05$ μAcm^{-2}, the coupled HH cells fire a single spike while being synchronized and then reach the resting potential. Figure 4b shows the activation of the Na+ gate, and Figure 4c and Figure 4d show the activation and inactivation of the K+ and Na+ gates respectively for the given input current value, which behaves in line with the behavior of the membrane potential variable. The time–frequency response of the STFT of the membrane potential, Na+ activation, K+ activation and Na+ inactivation gates is shown in Figure 4e, Figure 4f, Figure 4g and Figure 4h respectively. The brighter red area in the spectrogram image shows the frequency that has the maximum power. One can see from the spectrograms using the STFT that the frequency is at maximum power only at the time of single-spike generation; after that there is no high-frequency activity due to the lack of oscillation. The scalogram using the CWT of the firing spike and the Na+ activation gate, K+ activation gate, and Na+ inactivation gate is shown in Figure 4i, Figure 4j, Figure 4k, and Figure 4l respectively. The bright reddish hue in the image confirms that high-energy frequency activity occurs only at the time of single-spike generation; after that no frequency activity takes place.

Figure 5 shows the evolution path of state variables (membrane voltage V, Na+ activation gate m, Na+ inactivation gate h and K+ activation gate n) in phase portraits. The time evolution of the synchronization performance of coupled oscillators in the single-spike regime shown in Figure 6 shows that during spiking time there is small fluctuation in the error norm in the order of 10^{-4} in the log scale, and with time the synchronization error in both the Frobenius norm and L_2 norm plots decreases below the order of 10^{-10} in the log scale.

Here, Figure 5 shows the state-space excursion associated with the single action potential. Although the projected trajectory forms a large loop, it is not repeatedly traversed and therefore should not be interpreted as a sustained limit cycle. Instead, the loop represents the transient excursion during the spike followed by relaxation toward the terminal equilibrium region. This is consistent with Figure 4, where only one action potential is observed, and with Figure 6, where the synchronization errors subsequently decrease to very small values.

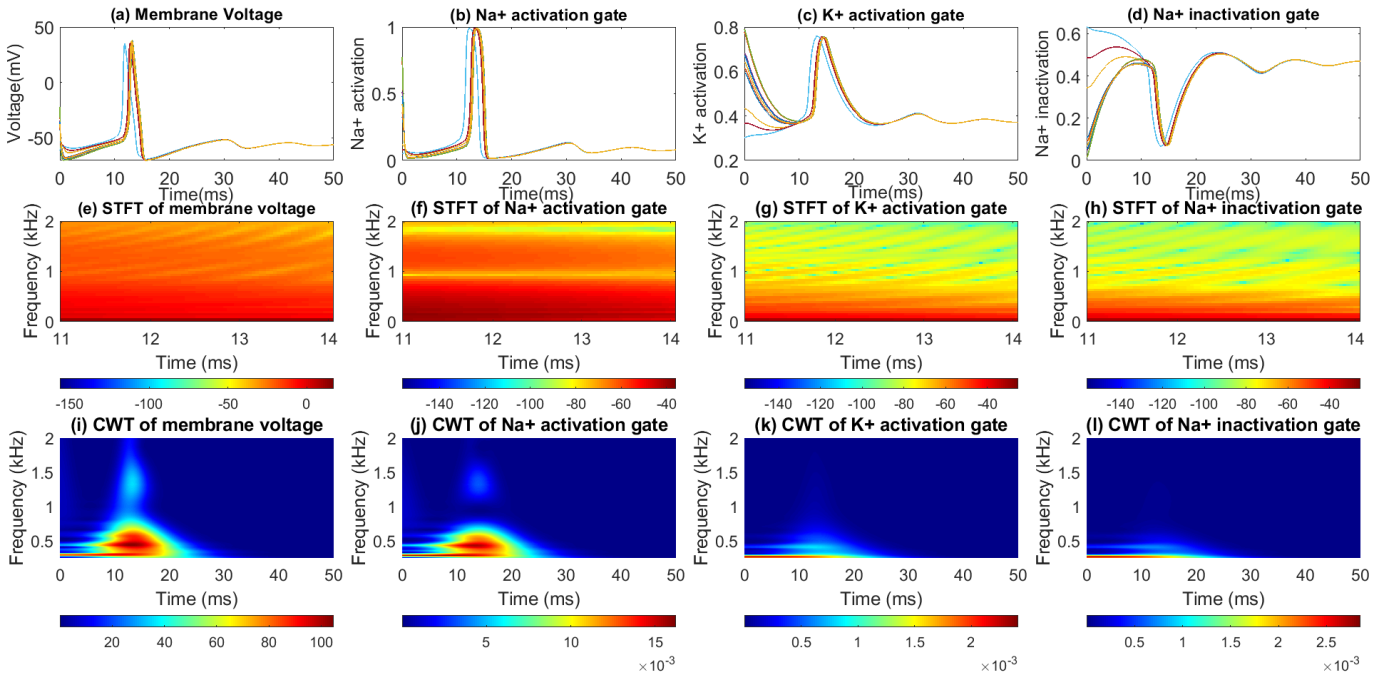


Figure 4. For a network of $N = 25$ coupled HH neurons and input current $I = 0.05$ μA cm^{-2}: (**a**) membrane voltage vs. time; (**b**) Na+ activation gate vs. time; (**c**) K+ activation gate vs. time; (**d**) Na+ inactivation gate vs. time; (**e**) STFT of membrane voltage; (**f**) STFT of Na+ activation gate; (**g**) STFT of K+ activation gate; (**h**) STFT of Na+ inactivation gate; (**i**) CWT of membrane voltage; (**j**) CWT of Na+ activation gate; (**k**) CWT of K+ activation gate; (**l**) CWT of Na+ inactivation gate.

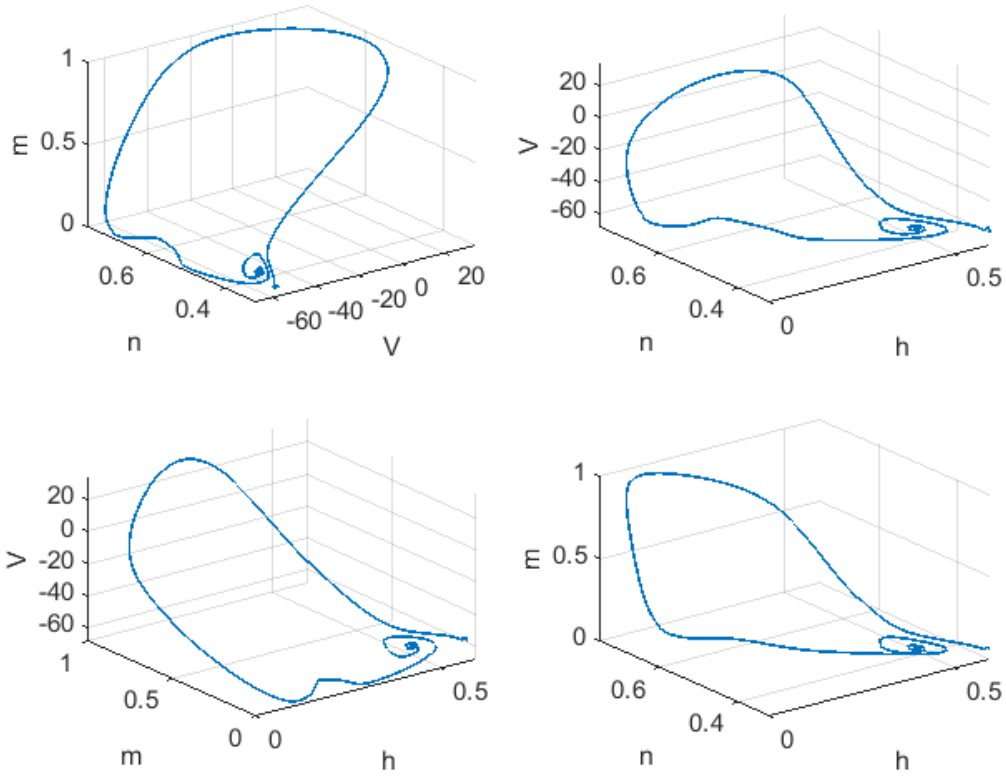


Figure 5. Phase portraits of neural signal when input current $I = 0.05$ μAcm^{-2}; M—membrane voltage; m—Na+ activation gate; n—K+ activation gate; h—Na+ inactivation gate.

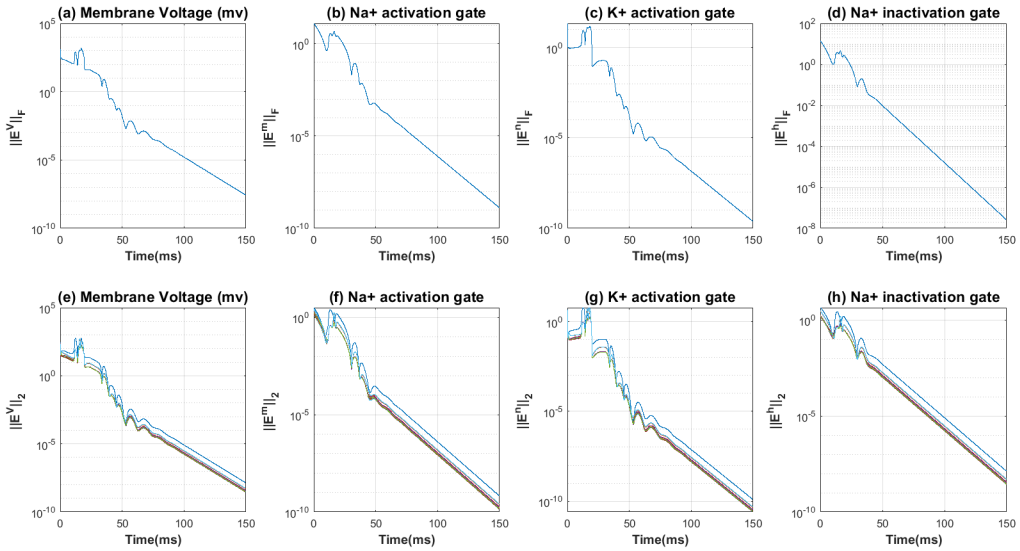


Figure 6. Synchronization error in Frobenius norm and L_2 norm logarithmic scales for input current $I = 0.05$ μAcm^{-2}.

3.3. Regular Firing Regime

Here, we studied the synchronization of coupled HH cells in a regular firing regime. Figure 7 shows that for input stimulus current $I = 0.07$ μAcm^{-2} the ensemble of coupled HH cells starts regular firing. Figure 7a shows how the coupled HH cells are synchronized from the desynchronized state and fire together at the same time. Figure 7b–d show activation of the Na+ and K+ gates and inactivation of the Na+ gate over time. The frequency response of the STFT of membrane voltage and the Na+ activation gate, K+ activation gate and Na+ inactivation gate is shown in Figure 7e, Figure 7f, Figure 7g, and Figure 7h respectively. The reddish hue at the output image shows the frequency of highest strength. The frequency response of the CWT of membrane voltage, Na+ and K+ activation gates, and Na+ inactivation gate is shown in Figure 7i, Figure 7j, Figure 7k, and Figure 7l respectively.

Figure 8 shows the evolution path of state variables of membrane voltage V, Na+ activation gate m, Na+ inactivation gate h and K+ activation gate n via phase portraits for input current $I = 0.07$ μAcm^{-2}. The occurrence of a limit cycle confirms that the system generates periodic outputs. The shape of the non-uniform limit cycle signifies that the system is nonlinear. The stable limit cycle also confirms that in the phase space, all the neighboring trajectories approach the limit cycle as the time approaches infinity. The time evolution of the synchronization performance of coupled oscillators in the regular firing regime shown in Figure 9 indicates that there is small fluctuation in both the Frobenius norm and L_2 norm plots in the order of 10^{-2} in the log scale, and with time the synchronization error decreases below the order of 10^{-5} in the log scale.

The repeatedly traversed closed trajectories in Figure 8 are consistent with the sustained periodic firing observed in Figure 7. In contrast to the single-spike trajectory of Figure 5, similar portions of the state-space trajectory are revisited during successive spikes. Figure 9 further shows that the pairwise synchronization errors decrease overall, although small oscillatory variations remain during the rapid spike transitions. We therefore interpret Figures 7–9 as numerical evidence of recurrent synchronized activity over the investigated time interval, without making a stronger claim concerning global attraction for arbitrary initial conditions.

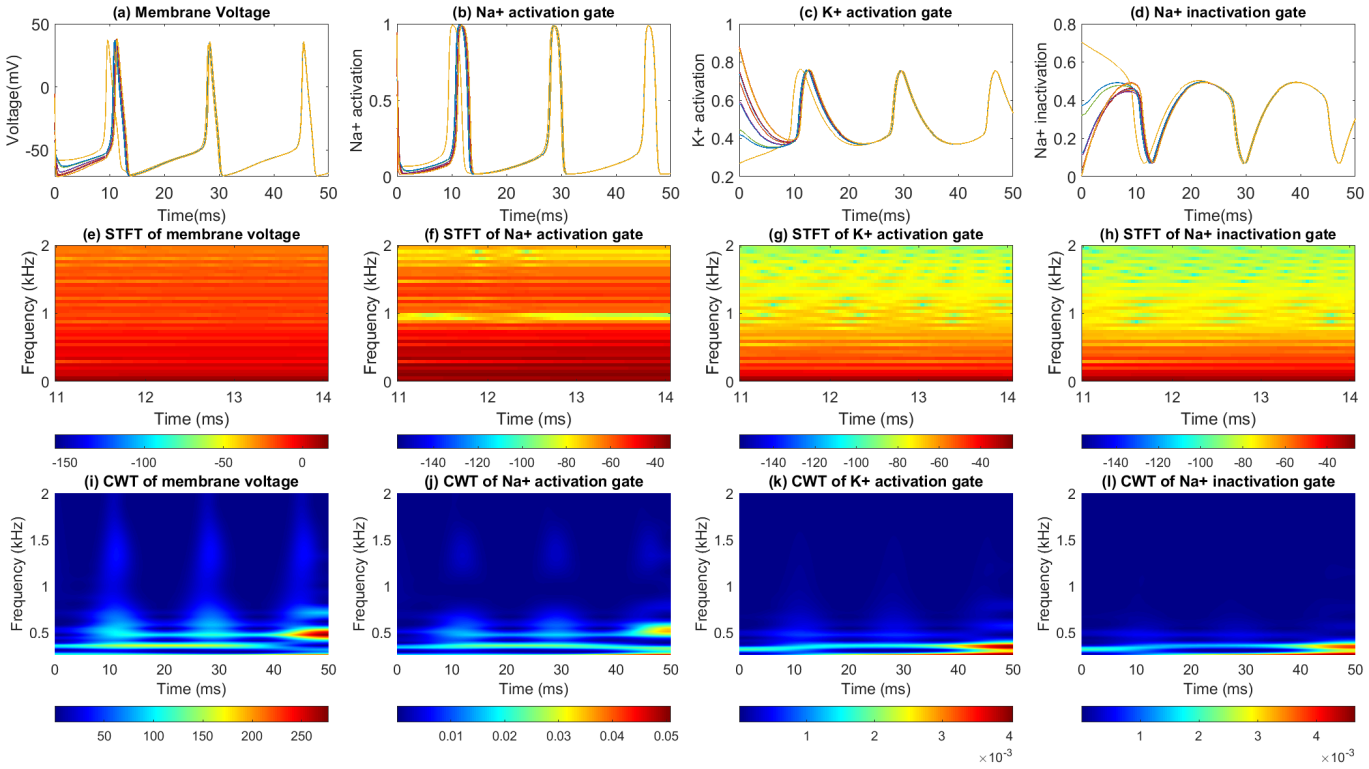


Figure 7. For input current I = 0.07 μAcm^{-2}: (**a**) membrane voltage vs. time; (**b**) Na+ activation gate vs. time; (**c**) K+ activation gate vs. time; (**d**) Na+ inactivation gate vs. time; (**e**) STFT of membrane voltage; (**f**) STFT of Na+ activation gate; (**g**) STFT of K+ activation gate; (**h**) STFT of Na+ inactivation gate; (**i**) CWT of membrane voltage; (**j**) CWT of Na+ activation gate; (**k**) CWT of K+ activation gate; (**l**) CWT of Na+ inactivation gate.

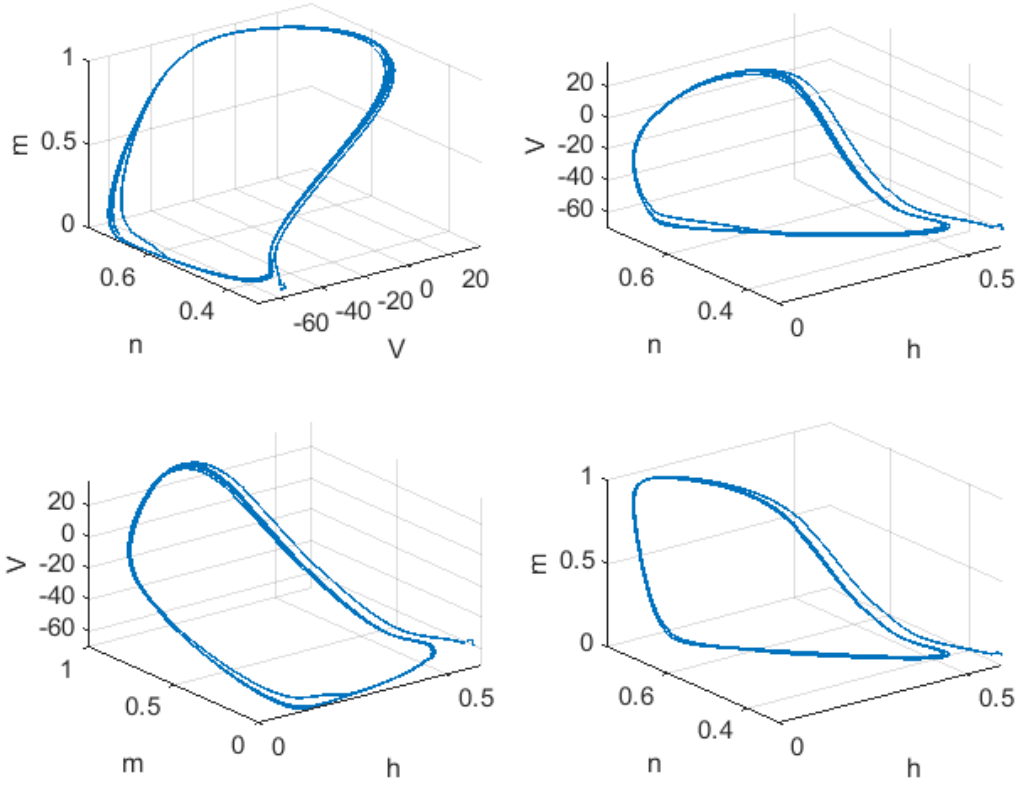


Figure 8. Phase portraits of neural signal when input current I = 0.07 μAcm^{-2}; M—membrane voltage; m—Na+ activation gate; n—K+ activation gate; h—Na+ inactivation gate.

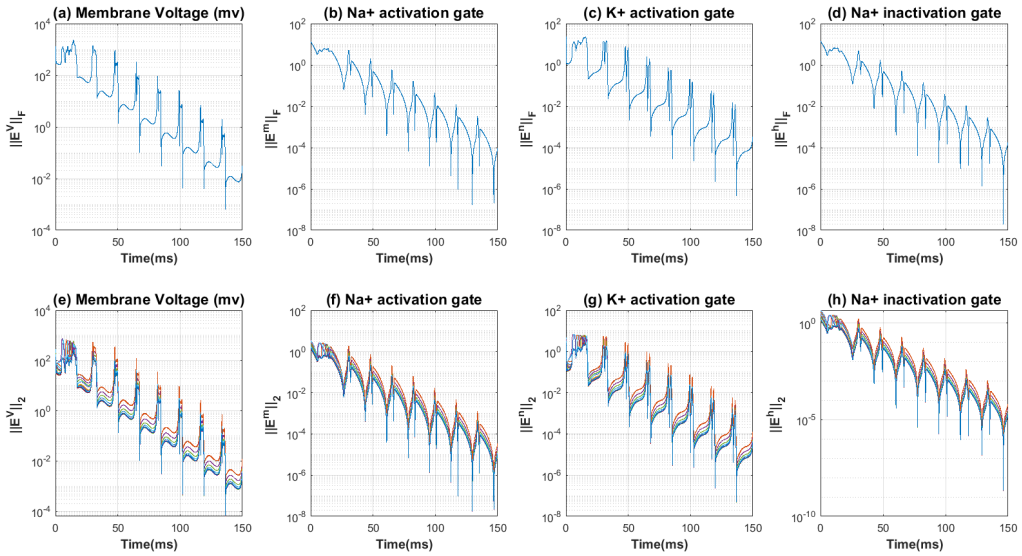


Figure 9. Synchronization error in Frobenius norm and L_2 norm logarithmic scales for input current $I = 0.07$ μAcm^{-2}.

3.4. Dephasing and Bursting

Here, we show that for input current $I = 0.1$ μAcm^{-2} the coupled HH cells exhibit a complex time phenomenon of dephasing and firing without help of any external factor. Han et al. [40] reported similar behavior of coupled neural oscillators using Morris Lecar system. Here, we observe this complex time behavior of coupled oscillators using coupled HH cells. The finite-time pattern is referred to here descriptively as bursting. Figure 10a shows that at coupling strength $k = 0.7$ and input stimulus current $I = 0.01$, coupled HH cells are desynchronized at the beginning, leading to the dephasing state, and then after a while they start firing synchronously. Figure 10b–d show the similar behaviors of the Na+ activation gate, K+ activation gate and Na+ inactivation gate in the time scale. Figure 10e, Figure 10f, Figure 10g and Figure 10h show the STFT response of firing spikes, the Na+ activation gate, the K+ activation gate and the Na+ inactivation gate respectively. The reddish hue regions in the figures of the STFT output show the frequencies that have maximum strength. Figure 10i, Figure 10j, Figure 10k and Figure 10l show the CWT values of bursting spikes and the Na+ activation, K+ activation and Na+ inactivation gates respectively.

Figure 11 shows the temporal evolution of state variables of membrane voltage V, Na+ activation gate m, Na+ inactivation gate h and K+ activation gate n via the phase portraits. The limit cycles in the phase portraits show that the spikes fire in a periodic fashion, and the trajectories are consistent with recurrent firing over the simulated interval. But the appearance of the small sink node indicates that the system enters the dephasing state before firing periodically again. Any initial value of the state variables in the phase space is attracted into the periodic orbits. The time evolution of the synchronization performance of coupled oscillators in the dephasing and bursting regimes shown in Figure 12 indicates that at the dephasing time there is no fluctuation in either the Frobenius norm or L_2 norm plots. The small fluctuations appear in both the error norms, and with time, both the synchronization errors decrease below the order of 10^{-2} in the log scale. The recurrent trajectories are consistent with periodic firing over the simulated interval. Hence, no conclusion concerning global attraction from arbitrary initial conditions is inferred from these finite-time phase portraits.

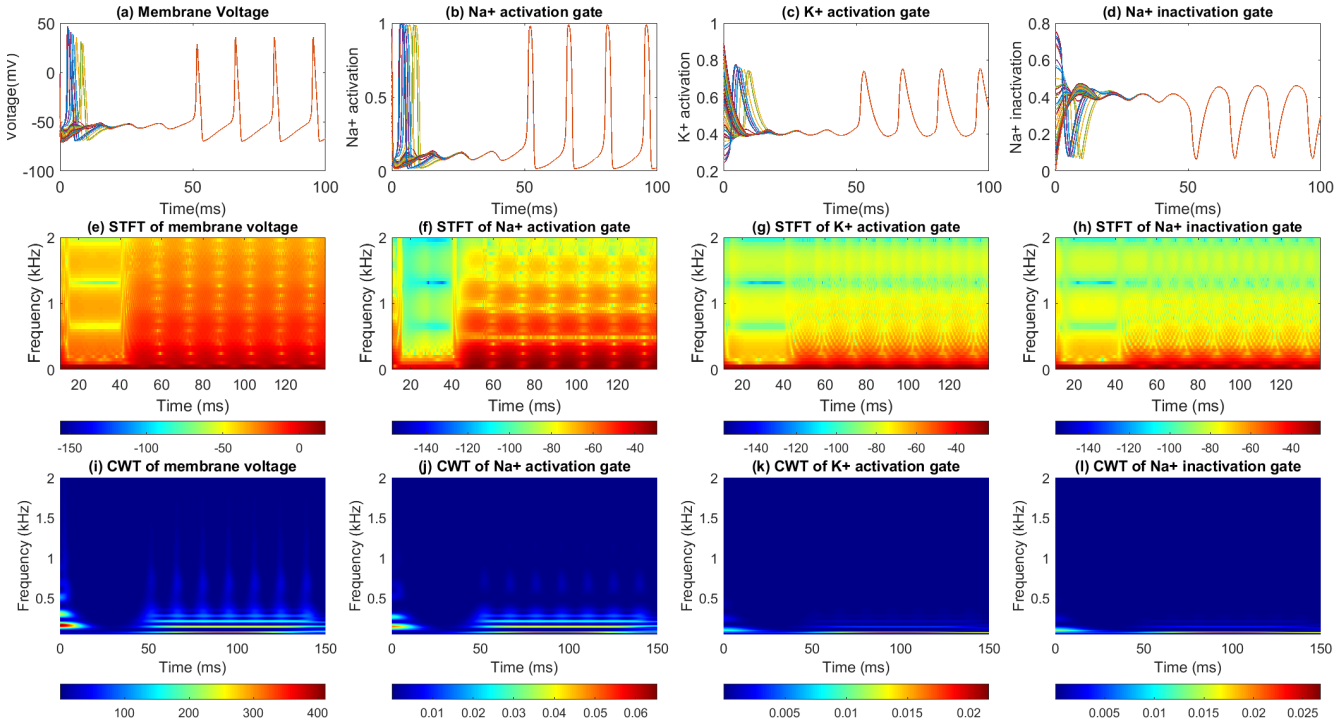


Figure 10. For input current $I = 0.1$ μAcm^{-2} and coupling strength $k = 0.7$: (**a**) membrane voltage vs. time; (**b**) Na+ activation gate vs. time; (**c**) K+ activation gate vs. time; (**d**) Na+ inactivation gate vs. time; (**e**) STFT of membrane voltage; (**f**) STFT of Na+ activation gate; (**g**) STFT of K+ activation gate; (**h**) STFT of Na+ inactivation gate; (**i**) CWT of membrane voltage; (**j**) CWT of Na+ activation gate; (**k**) CWT of K+ activation gate; (**l**) CWT of Na+ inactivation gate.

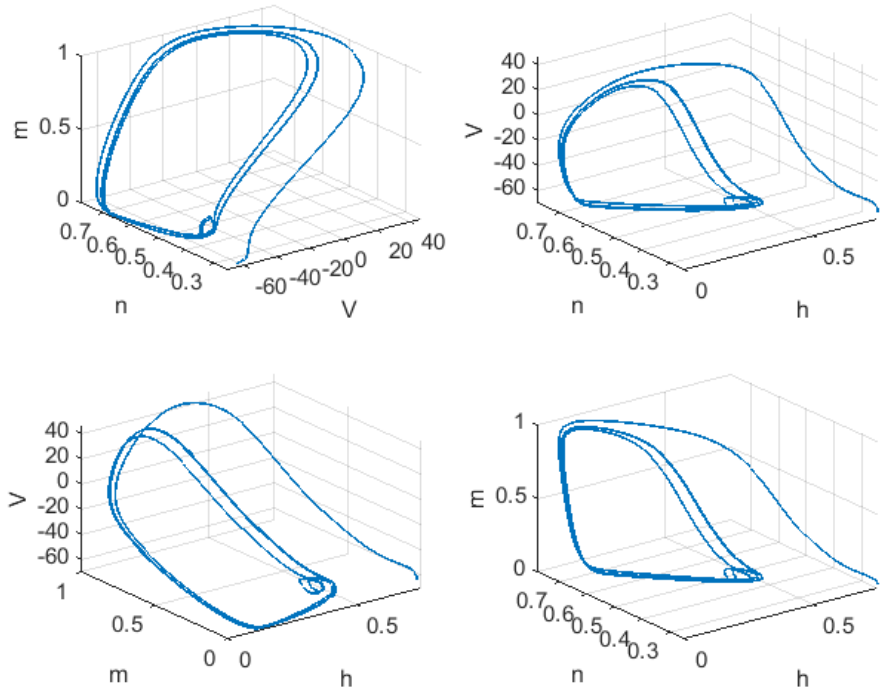


Figure 11. Phase portraits of neural signal when input current $I = 0.1$ μAcm^{-2} and coupling strength $k = 0.7$; M—membrane voltage; m—Na+ activation gate; h—Na+ inactivation gate; n—K+ activation gate.

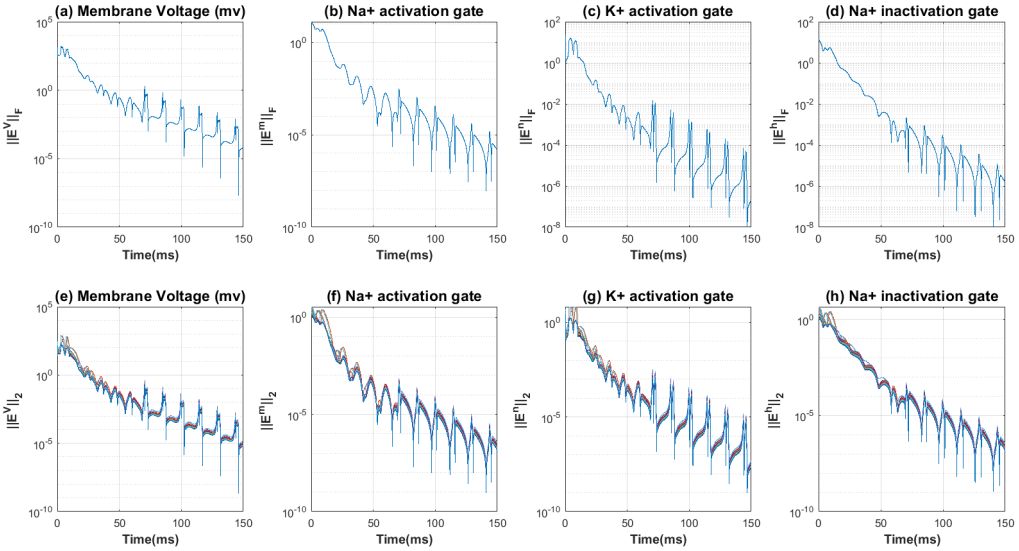


Figure 12. Synchronization error in Frobenius norm and L_2 norm logarithmic scales for input current $I = 0.1$ μAcm^{-2} and coupling strength $k = 0.7$.

Here, the term "bursting" is used descriptively for the finite-time pattern observed in the simulated response rather than as a formal slow–fast bursting classification. The principal observation relevant to the present study is the transition from initially dispersed trajectories to more coordinated recurrent firing.

3.5. Dephasing Regime

For the comparatively high input current $I = 1.5$ μAcm^{-2}, the coupled HH cells exhibit the response referred to here as the dephasing regime. The coupled HH cells are not synchronized at the beginning. They start to be synchronized but dephase out at the same time. Figure 13a, Figure 13b, Figure 13c and Figure 13d exhibit the synchronizing and dephasing out of the firing spikes, activation of the Na+ gate, activation of the K+ gate and inactivation of the Na+ gate, respectively. The frequency response of the STFT of firing spikes, the Na+ and K+ activation gates and the Na+ inactivation gate is shown in Figure 13e–h, which indicate the different frequency components present at each time window. The frequency with maximum spectral power is denoted by the reddish hue in the image. Similarly, the frequency response of the CWT of firing spikes, the Na+ and K+ activation gates and the Na+ inactivation gate is shown in Figure 13i–l, where the x-axis gives the time information, the y-axis gives the frequency response and the color code indicates the strength of the frequency components.

Figure 14 shows the finite-time state-space evolution of the membrane voltage and gating variables for $I = 1.5$ μAcm^{-2}. The trajectories contract toward a relatively small terminal region over the simulated interval, which is consistent with the damped response observed in the corresponding time series. This finite-time behavior is not interpreted here as a formal demonstration of global asymptotic stability or attraction for arbitrary initial conditions. The time evolution of the synchronization performance of coupled oscillators in the dephasing regime, as shown in Figure 15, shows that there is small fluctuation in both the Frobenius norm and L_2 norm plots in order of 10^{-5} in the log scale, and with time the synchronization error decreases below the order of 10^{-10} in the log scale.

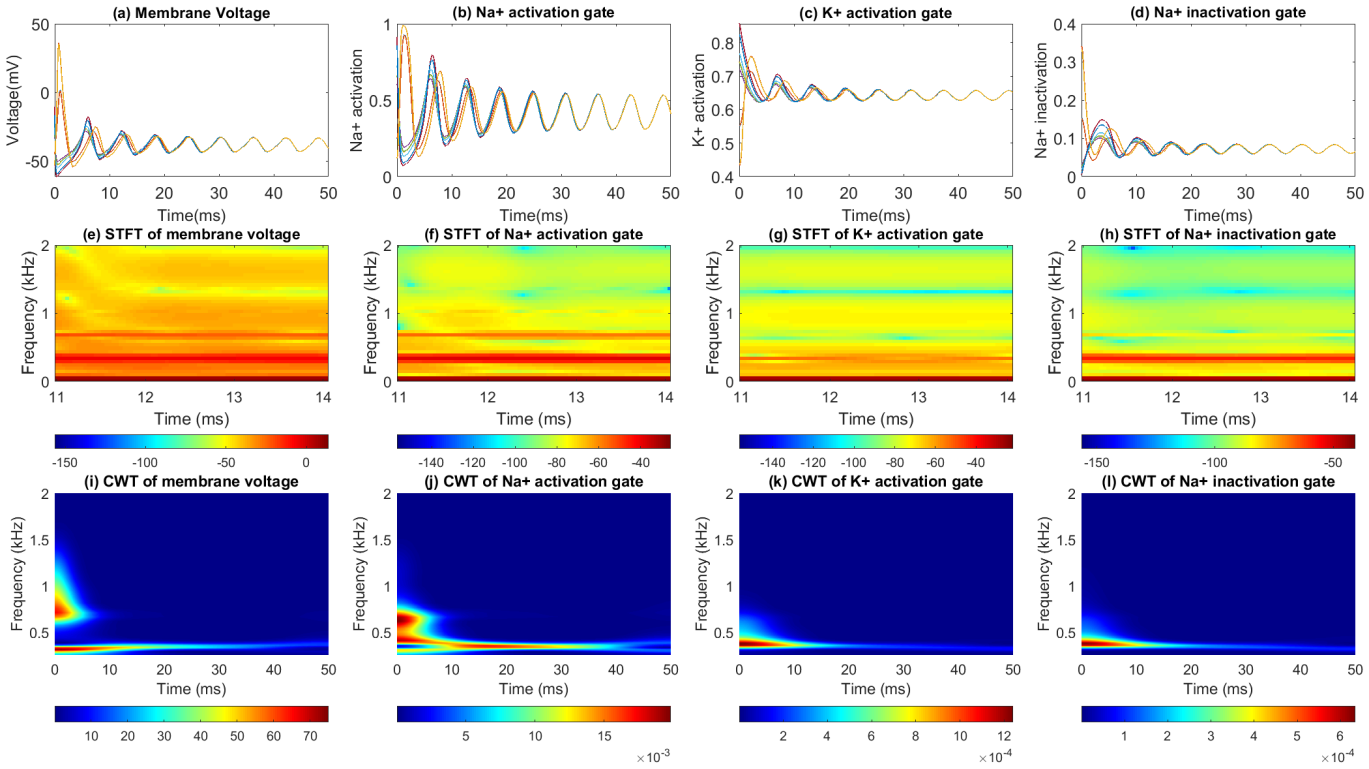


Figure 13. For input current I = 1.5 μAcm^{-2}: (**a**) membrane voltage vs. time; (**b**) Na+ activation gate vs. time; (**c**) K+ activation gate vs. time; (**d**) Na+ inactivation gate vs. time; (**e**) STFT of membrane voltage; (**f**) STFT of Na+ activation gate; (**g**) STFT of K+ activation gate; (**h**) STFT of Na+ inactivation gate; (**i**) CWT of membrane voltage; (**j**) CWT of Na+ activation gate; (**k**) CWT of K+ activation gate; (**l**) CWT of Na+ inactivation gate.

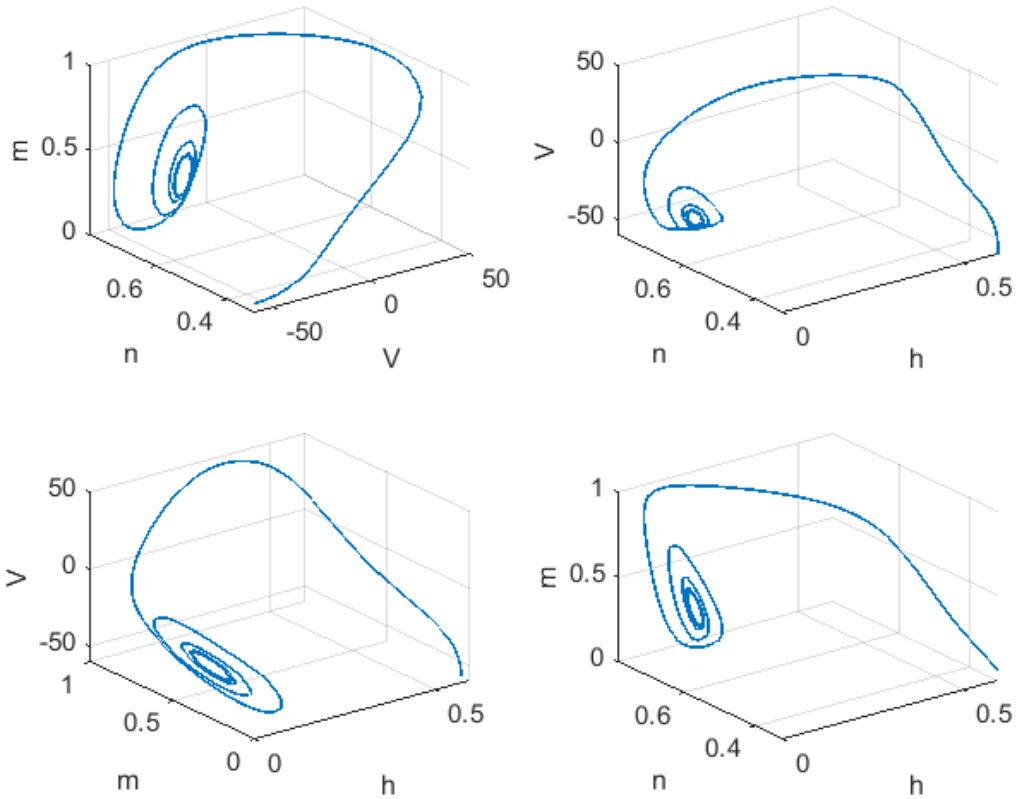


Figure 14. Phase portraits of neural signal when input current I = 1.5 μAcm^{-2} ; M—membrane voltage; m —Na+ activation gate; n—K+ activation gate; h—Na+ inactivation gate.

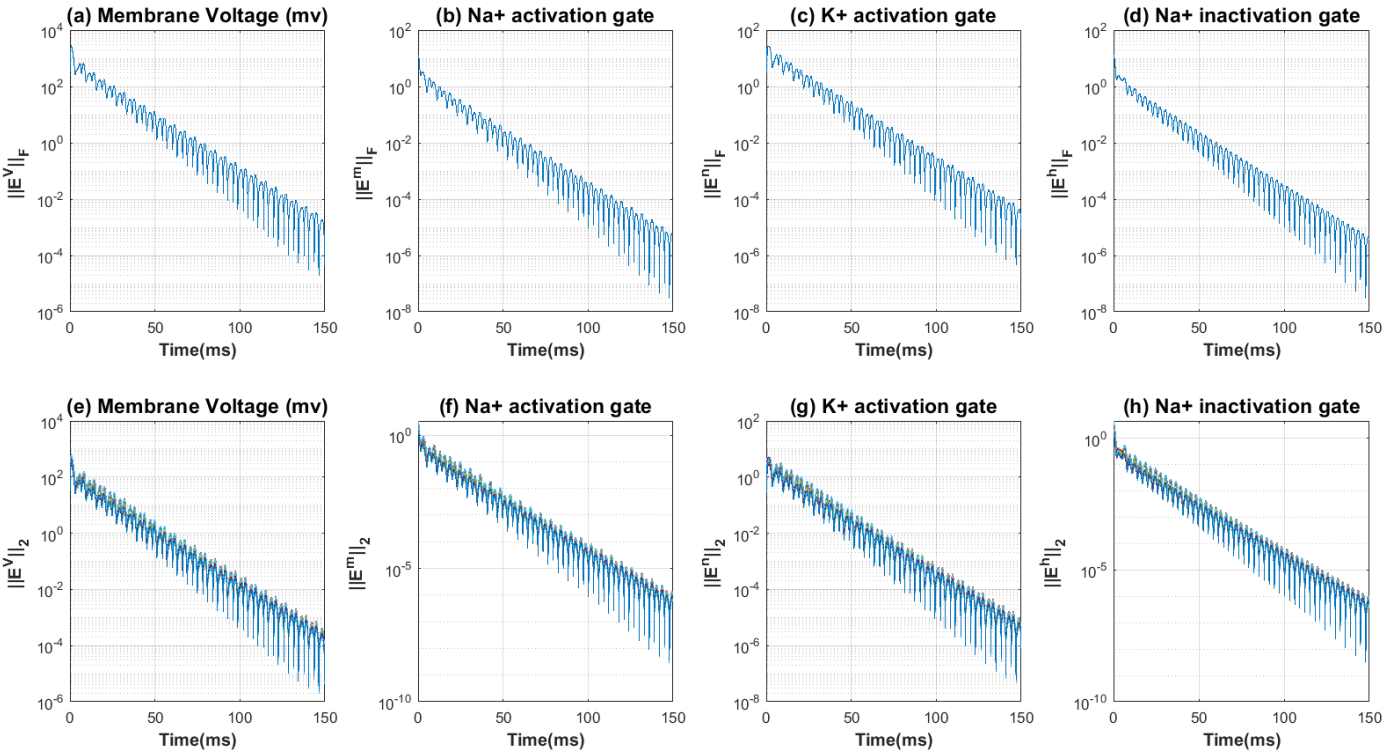


Figure 15. Synchronization error in Frobenius norm and L_2 norm logarithmic scales for input current $I = 1.5\ \mu\text{Acm}^{-2}$.

3.6. Firing Frequency and Input Current Relation in Coupled HH Cells

Here, we obtained the dominant firing frequency of coupled HH cells for various input currents and plotted them together. Figure 16 shows the dynamics of stimulus current vs. firing frequency of the coupled HH cells. Figure 16 shows that with the increase in input current the firing frequency is also increased. So, we infer that coupled neuron cells exhibit one different spiking regime of dephasing and bursting compared to a single neuron with an increase in the input current. But the firing frequency of the synchronized coupled neuron cells increases similarly to the single neuron with an increase in input current. So our result indicates that if the supplied input current to an ensemble of coupled neurons increases, the neurons fire in higher frequencies. This situation models the modulatory effects of adaptive current in the brain [41].

Across the sampled current values, the dominant spectral component estimated from the voltage and gating-variable responses generally increases with applied current. Since the investigated currents are discrete representative operating points rather than a dense bifurcation sweep, this relationship is reported as an empirical trend over the sampled parameter values rather than as a complete current–frequency characteristic of the coupled HH network.

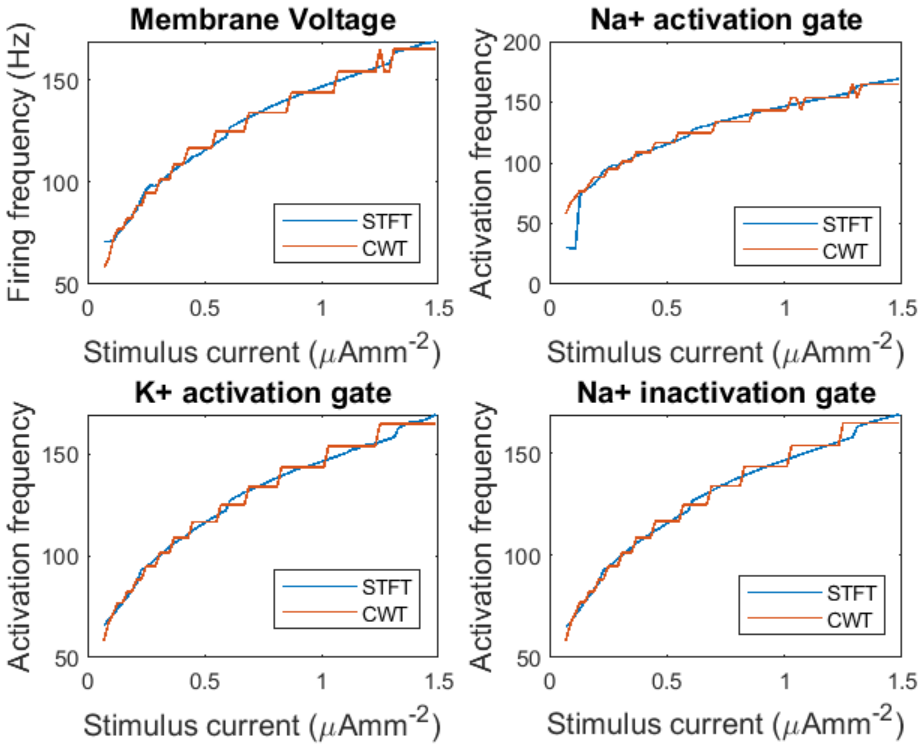


Figure 16. Relation between membrane-voltage firing, Na+ gate activation, K+ gate activation and Na+ gate inactivation vs. input stimulus current.

4. Frequency Response Analysis of Coupled HH Cells for Variation in Coupling Strength

One of the instrumental parameters of coupled HH cells is their coupling strength. Strongly coupled cells synchronize more quickly than the weakly coupled ones. We studied the synchronization of coupled HH cells for varying strength of coupling parameters. We took a model of $N = 25$ coupled HH cells. We set the initial membrane voltage of the coupled HH cells as uniformly distributed random numbers in the interval of $(-60, 0)$ mV. To determine the impact of coupling strength on synchronization, we perturbed the HH cells in the system with input stimulus current equal to $I = 0.07$ µAcm^{-2} so that the cells entered the regular firing regime.

4.1. Weakly Coupled HH Cells

Here, we studied the coupled system when HH cells are weakly coupled or the value of the coupling is low. The spike dynamics of coupled HH cells with coupling strength $k = 0.1$ are shown in Figure 17. First, Figure 17a shows the time series of firing spikes, then Figure 17b–d show the dynamics of the Na+ activation gate, K+ activation gate and Na+ inactivation gate over time. These figures show that the HH cells are initially desynchronized and then they are synchronized over time. Figure 17e–h show the behavior of the STFT response of firing spikes and Na+ activation, K+ activation and Na+ inactivation gates over time. As shown in the figures the whole time series of the total simulation was broken into smaller windows, and then for each window, the STFT was calculated. The different color blocks in each window show the different frequency components present in the signal. The reddish hue shows the frequency, which has the maximum spectral power. Next, Figure 17i, Figure 17j, Figure 17k, and Figure 17l show the CWT response of generated spikes, the Na+ activation gate, the K+ activation gate and the Na+ inactivation gate respectively. The reddish hue signifies the frequency with maximum strength.

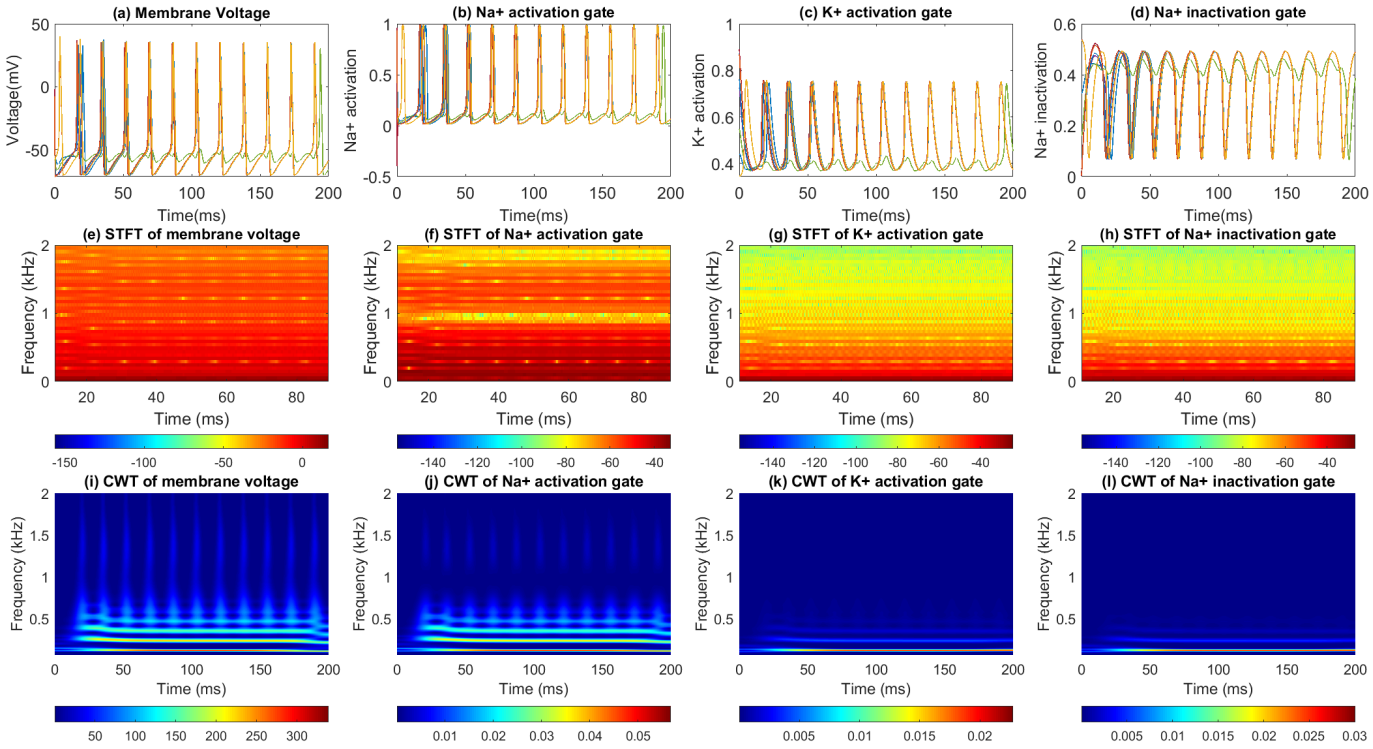


Figure 17. For a coupling strength of 0.1: (**a**) membrane voltage vs. time; (**b**) Na+ activation gate vs. time; (**c**) K+ activation gate vs. time; (**d**) Na+ inactivation gate vs. time; (**e**) STFT of membrane voltage; (**f**) STFT of Na+ activation gate; (**g**) STFT of K+ activation gate; (**h**) STFT of Na+ inactivation gate; (**i**) CWT of membrane voltage; (**j**) CWT of Na+ activation gate; (**k**) CWT of K+ activation gate; (**l**) CWT of Na+ inactivation gate.

Figure 18 shows the phase portraits of N coupled HH cells when coupling strength is as low as $k = 0.1$. The figures show the paths of evolution of state variables of membrane voltage V, Na+ activation gate m, Na+ inactivation gate h and K+ activation gate n. The recurrent closed trajectories in Figure 18 are consistent with the periodic firing observed in the corresponding time series over the simulated interval. Their non-circular shape reflects the nonlinear character of the HH dynamics. No stronger conclusion concerning global asymptotic stability is drawn from these finite-time projected trajectories. Also, the non-uniform shape of the limit cycle confirms that the system is nonlinear. The time evolution of the synchronized performance of coupled oscillators in the regular firing regime while they are loosely coupled is shown in Figure 19, which displays that there is fluctuation in both the Frobenius norm in the range of 10^3 to 10^0 in the log scale and L_2 norm plots in the order of 10^2 to 10^{-4} that quantitatively describes the lack of synchronization among the oscillator cells. To study further the behavior of coupled HH cells we generated raster plots from our coupled HH cell model. We first observe the pattern of synchronization of HH cells in the presence of low coupling strength over a period of 5 ms, which is shown via the raster plot in Figure 20. In the plot, the blue dots represent the peaks of the generated spikes over time for up to 200 cells. As seen in Figure 20, the spikes of the coupled cells are more dispersed and scattered and fire at an average frequency of 3.21 Hz, which reveals that they are less synchronized over time when coupling strength is low. It is also evident that for low coupling strength, some oscillator responses may not synchronize well over time, indicated by the horizontal gap, around oscillator number 60 in Figure 20.

The main information provided by Figure 20 is the dispersion of spike times across the population. The reported frequency value should not by itself be used to establish a coupling-dependent frequency trend because the raster plot covers only a short observation

interval. The dependence of the dominant spectral frequency on k is considered separately in Section 4.3 using the STFT and CWT estimates.

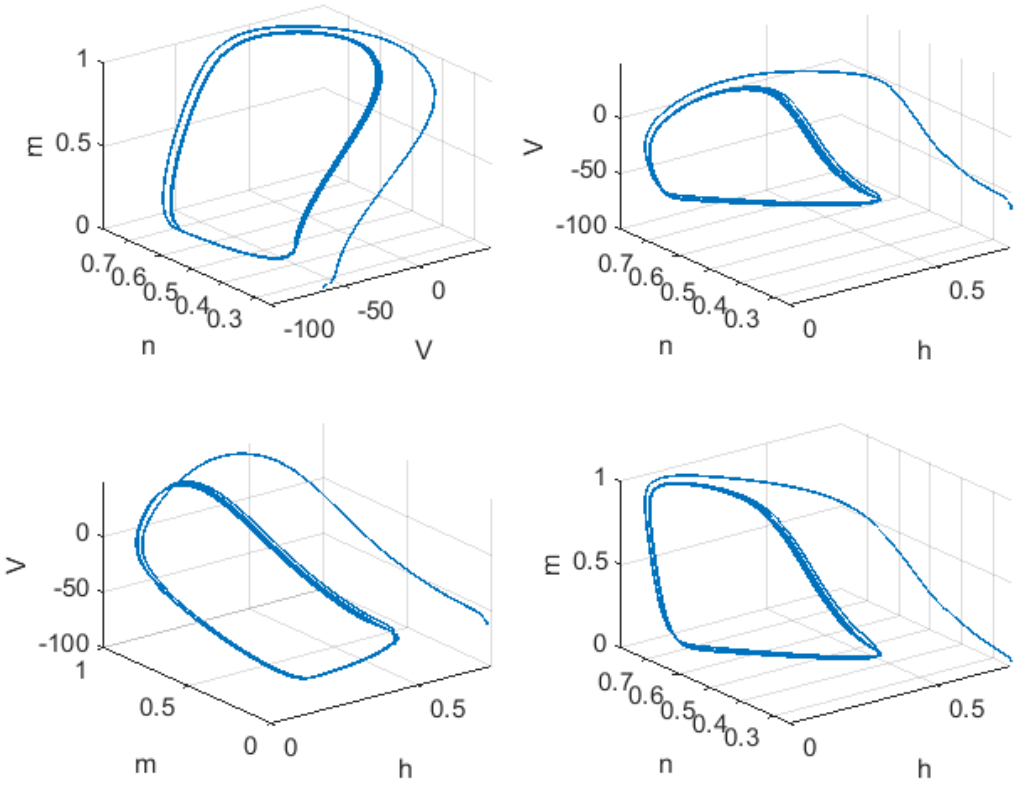


Figure 18. Phase portraits of neural signal when coupling strength 0.1; M—membrane voltage; m—Na+ activation gate; h—Na+ inactivation gate; n—K+ activation gate.

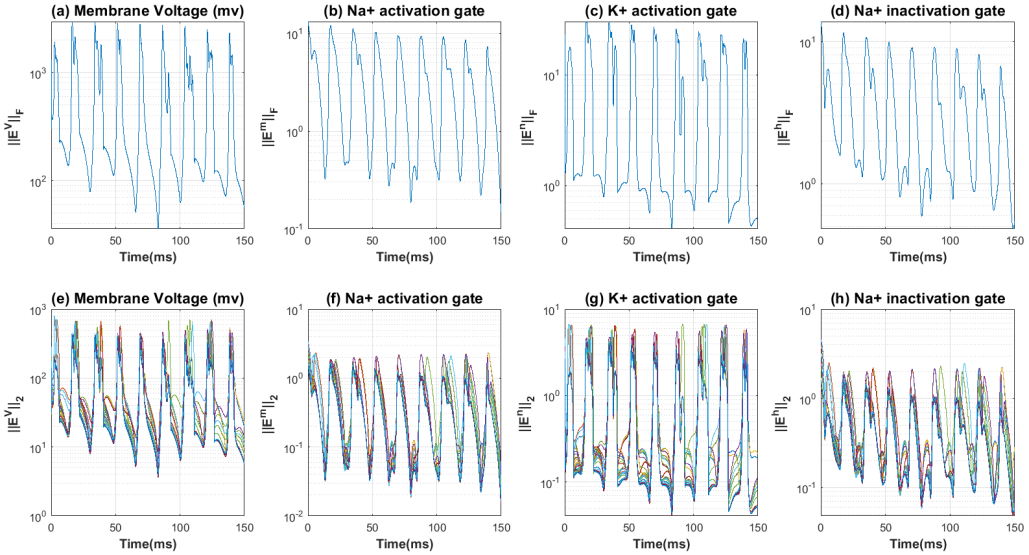


Figure 19. Synchronization error in Frobenius norm and L_2 norm logarithmic scales for input current $I = 0.07$ μAcm^{-2} and coupling strength as low as $k = 0.1$.

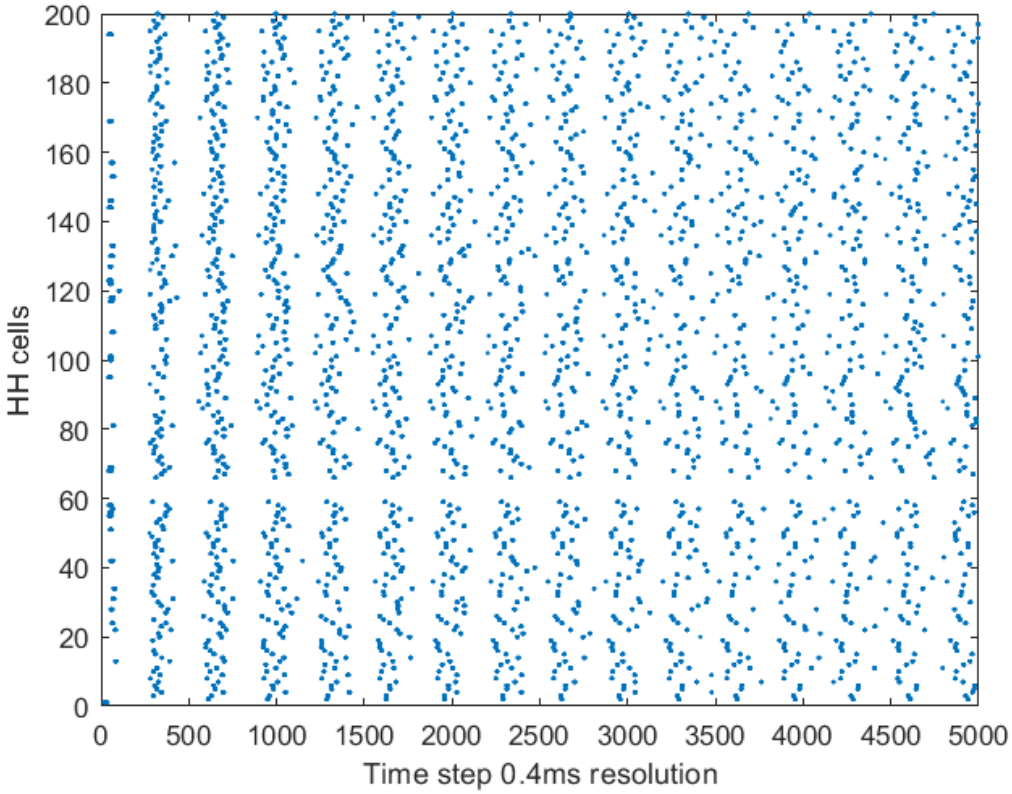


Figure 20. The raster plot shows the firing simulation of 200 coupled HH cells in the presence of low coupling strength over the period of 5ms. The HH cells fire in more dispersed mode in the presence of low coupling strength, and their average firing frequency is 3.21 Hz.

4.2. Strongly Coupled HH Cells

The dynamics of coupled HH cells for a coupling strength as high as $k = 0.9$ are shown in Figure 21. Here, Figure 21a shows the time series of spike firings, whereas Figure 21b–d show the dynamics of the Na+ activation, K+ activation and Na+ inactivation gates over time. It is visible from the figures that the spikes are highly synchronized and fire at the same time compared to the weakly coupled HH cells shown in the previous section. Figure 21e, Figure 21f, Figure 21g, and Figure 21h show the STFT response of firing spikes, the Na+ activation gate, the K+ activation gate and the Na+ inactivation gate respectively. The reddish hue in the figures of the STFT output shows the frequencies that have maximum spectral power. Figure 21i, Figure 21j, Figure 21k, and Figure 21l show the CWT values of bursting spikes and the Na+ activation, K+ activation and Na+ inactivation gates respectively.

Figure 22 shows the path of evolution of state variables of membrane voltage V, Na+ activation gate m, Na+ inactivation gate h and K+ activation gate n in the phase portraits. The limit cycles in the phase portraits show that the spikes fire periodically, leading to a stable response. The projected trajectories in Figure 22 are consistent with recurrent firing under the stronger coupling condition. Together with the decreasing synchronization-error measures in Figure 23, they indicate stronger finite-time alignment of the simulated cells than in the weak-coupling case. The phase portraits are not used to infer attraction from arbitrary initial conditions. The time evolution of the synchronization performance of coupled oscillators in the regular firing regime while strongly coupled is shown in Figure 23, which displays that there is small fluctuation in the Frobenius norm of the order 10^{-3} and L_2 norm plots of the order 10^{-4} in the log scale, which verifies that with time the synchronization error decreases below the order of 10^{-8} in the log scale and quantitatively confirms that the cells are strongly synchronized.

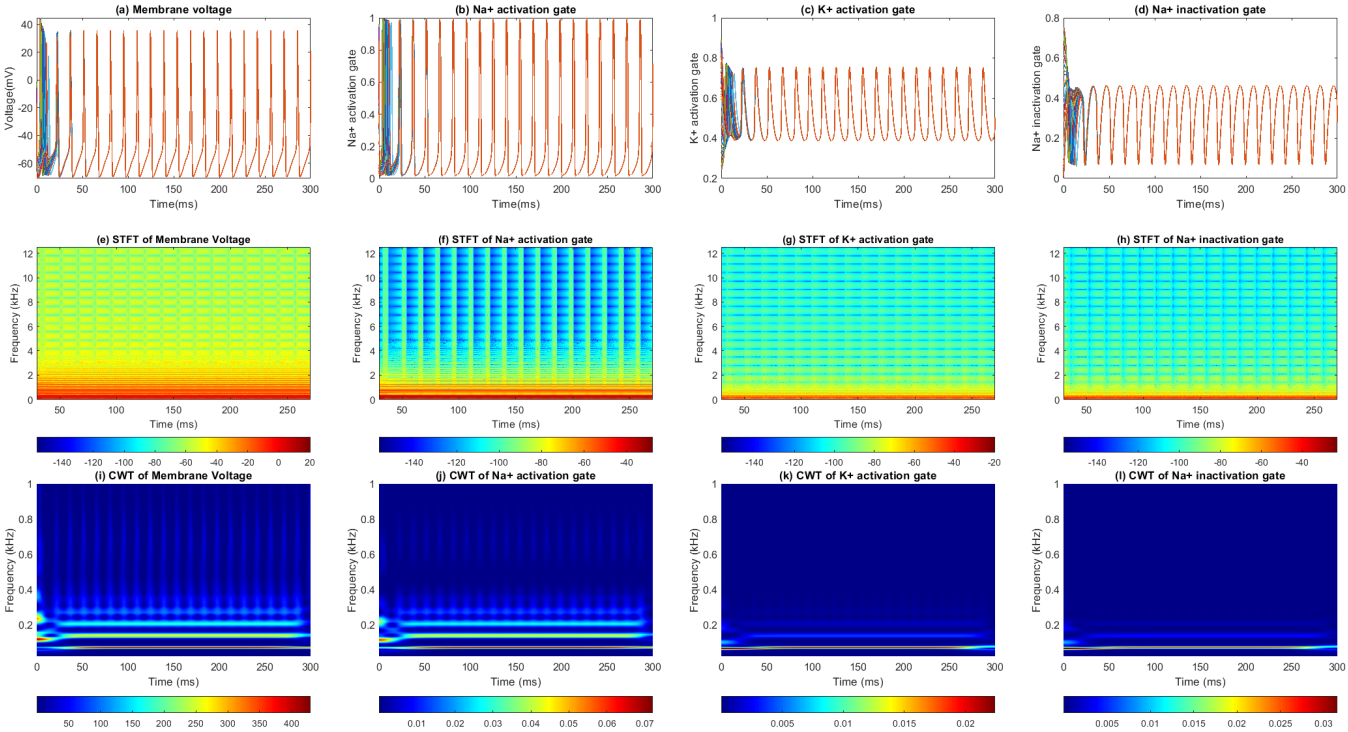


Figure 21. For a coupling strength of 0.9: (**a**) membrane voltage vs. time; (**b**) Na+ activation gate vs. time; (**c**) K+ activation gate vs. time; (**d**) Na+ inactivation gate vs. time; (**e**) STFT of membrane voltage; (**f**) STFT of Na+ activation gate; (**g**) STFT of K+ activation gate; (**h**) STFT of Na+ inactivation gate; (**i**) CWT of membrane voltage; (**j**) CWT of Na+ activation gate; (**k**) CWT of K+ activation gate; (**l**) CWT of Na+ inactivation gate.

In a continuation of our raster plot study, here we show the simulation pattern of the coupled HH cells in the presence of high coupling strength via the raster plot in Figure 24. As seen in Figure 24, the coupled cells all fire at the same time, which indicates that the cells are strongly coupled and fully synchronized when coupling strength is high. When computed, we find the firing frequency of strongly coupled HH cells to be 3.19 Hz, which is lower than the firing frequency of weakly coupled HH cells, which indicates that strongly coupled HH cells fire in a more synchronized way, but their firing frequency slowly diminishes. In Figure 24, we observe that the oscillator response is initially random and quickly latches in a right vertical alignment when the coupling strength is high unlike in Figure 20. It is to be noted that raster plots were recently used to quantify the frequency of spiking neurons [42] and the timing of working memory [43]. However, here our goal is to show the qualitative changes in raster plots for different coupling strengths in coupled HH cells, which have not been investigated before.

Comparison of Figures 20 and 24 provides clearer evidence for the effect of coupling strength on temporal alignment than on firing frequency. Increasing k produces a visibly narrower distribution of spike times. The small difference between the individual frequency values quoted for these two raster plots is not treated as sufficient evidence of a general frequency shift; this question is instead considered using the parameter sweep in Figure 25.

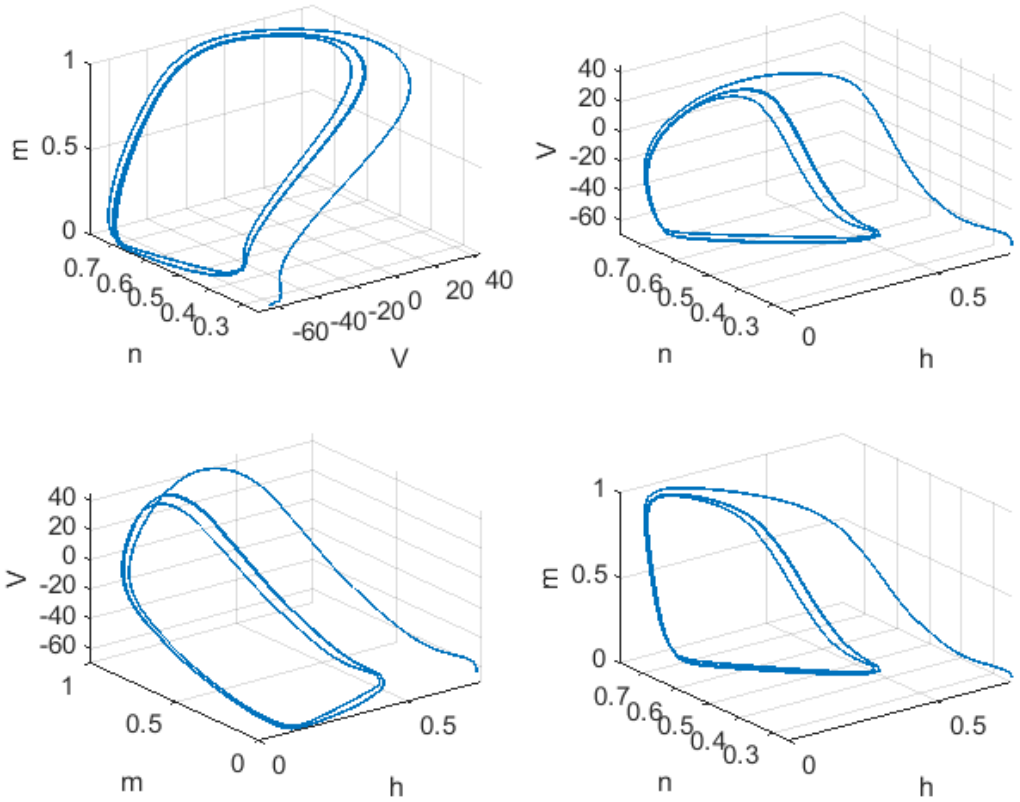


Figure 22. Phase portraits of neural signal when coupling strength = 0.9; *M*—membrane voltage; *m*—Na+ activation gate; *h*—Na+ inactivation gate; *n*—K+ activation gate.

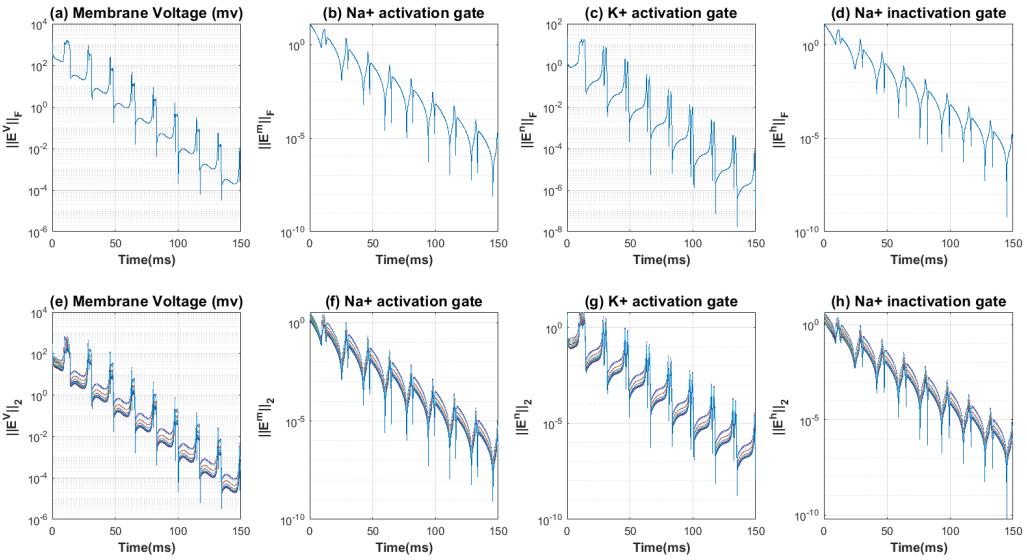


Figure 23. Synchronization error in Frobenius norm and L_2 norm logarithmic scales for input current $I = 0.07$ μAcm^{-2} and coupling strength as high as $k = 0.9$.

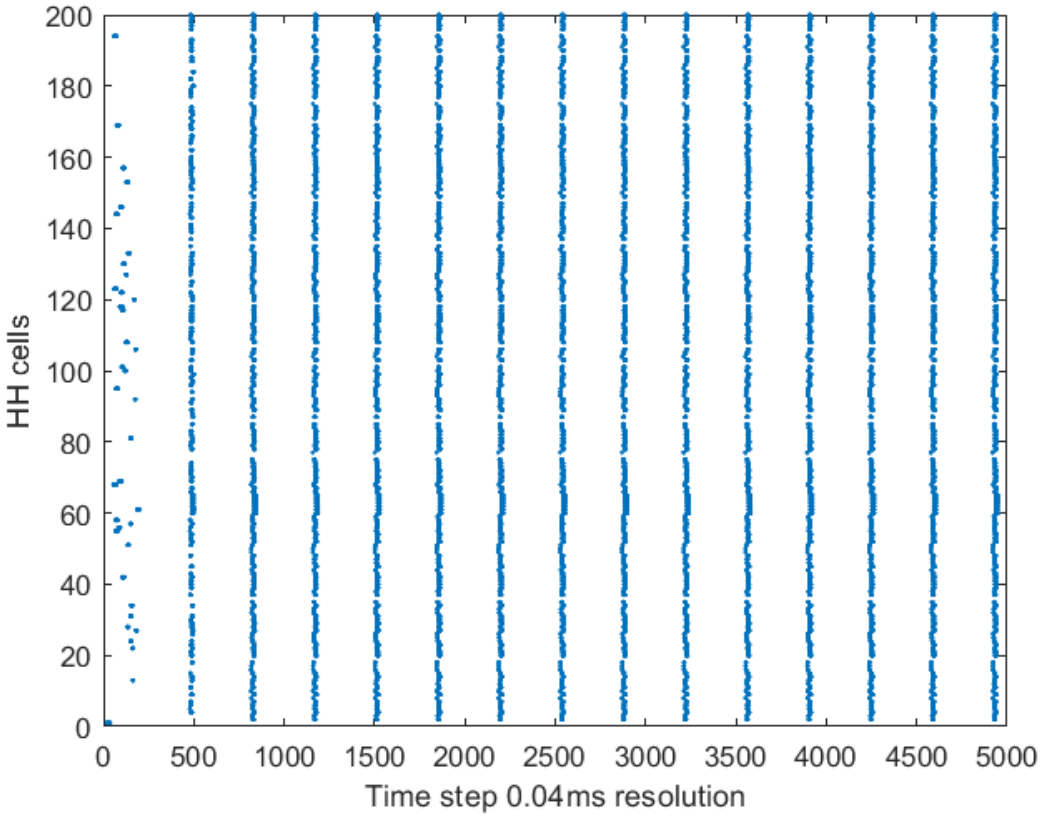


Figure 24. Raster plot of $N = 200$ coupled HH neurons under the high-coupling condition over the displayed 5 ms interval. The narrower vertical alignment of spike times indicates substantially stronger temporal coordination than in the weak-coupling case.

4.3. Finite-Time Dominant Frequency Estimates with Variation in Coupling Strength

Here, we examined how the normalized diffusive membrane-voltage coupling parameter k is associated with the dominant spectral component estimated from the finite simulated responses. We set the initial membrane voltage V values of all the HH cells using uniformly distributed random numbers in the interval of (-60,0) mV. In Figure 25a, we plotted the dominant firing frequency of membrane voltage V vs. the coupling strength k, for both the STFT and CWT. Similarly, in Figure 25b, Figure 25c and Figure 25d, we plotted the dominant firing frequency of the Na+ activation gate m, Na+ inactivation gate h and K+ activation gate n vs. coupling strength k respectively for both the STFT and CWT.

For the investigated finite network, initial conditions, simulation interval, and frequency-estimation procedure, the dominant spectral estimates in Figure 25 show a modest decreasing trend as k increases. This trend should be interpreted as an empirical result of the present numerical protocol. In particular, Equation (5) shows that the diffusive coupling term vanishes when all membrane voltages become identical. Therefore, the present results do not establish a universal mechanism by which stronger coupling must reduce the asymptotic intrinsic firing frequency of identical HH neurons. Changes in k also modify the synchronization transient and the waveform represented within the finite analysis window, both of which can affect the dominant spectral component extracted by the STFT or CWT. The more robust conclusion from Figures 17–25 is that increasing coupling promotes stronger temporal coordination, while a modest decreasing trend of the finite-time spectral estimate is observed under the numerical conditions studied here.

It is noteworthy that we chose 0.4 as the sampling time as an optimal trade-off between numerical stability and the volume of data generated through simulations. Further reduction in the step size increases the volume of data with no further improvement in

the synchronized waveforms. The numerical integration used the time step reported in Section 2.2. Because a systematic numerical step-size convergence study was not part of the present work, no claim is made that the results are completely independent of the chosen integration step. Furthermore, in Figure 25, we show the comparison of the dominant frequency using the CWT and STFT. It is found that the CWT always yields a monotonically decreasing pattern when coupling strength increases, whereas less robust estimation is obtained in the STFT. This is because the STFT has many tuning parameters like the point of FFT, signal length, and window. Therefore, the sharp changes are considered as noisy estimation for the STFT, showing that the CWT provides a smoother frequency trend for the present data, whereas the STFT estimates show greater variation because of their dependence on window length, overlap, and frequency resolution. Simulating at the specific coupling strengths involves a huge number of simulations of the networks and processing their waveforms. Since we observe a stable monotonic pattern in the CWT, it is not necessary to add more datapoints in between since it adds no extra information regarding how the dominant frequency changes with an increase in coupling strength. Similar to Figure 25, we see a noisier estimation using the STFT in Figure 16, where the CWT estimation gives a smoother upward pattern of the dominant frequency when the input current is increased. Here, the CWT provides a smoother frequency trend for the present data, whereas the STFT estimates show greater variation because of their dependence on window length, overlap, and frequency resolution. The two methods are therefore treated as complementary time–frequency representations rather than as independent evidence of synchronization.

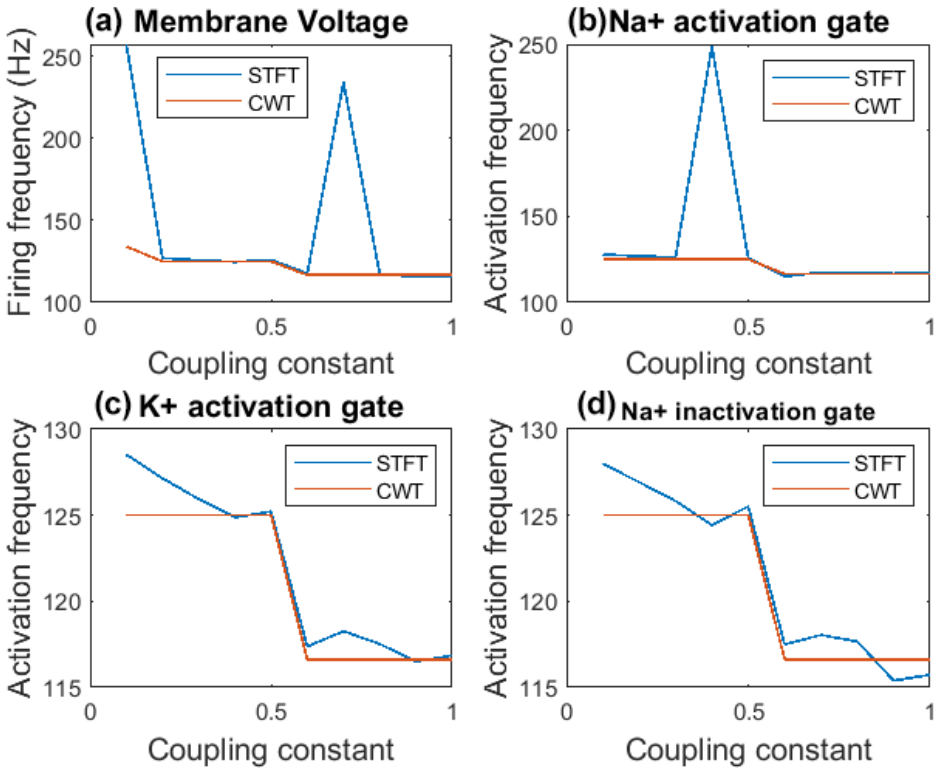


Figure 25. Relation between membrane-voltage firing, Na+ gate activation, K+ gate activation and Na+ gate inactivation frequencies vs. coupling strength.

5. Discussion and Limitations

Usually, the solution of oscillations generated from linear systems can be represented in terms of sinusoidal basis functions. In the present scenario, we deal with nonlinear oscillators since the governing equation has higher powers of n and m. This is also evident

from the asymmetric patterns of the phase portraits. However, these nonlinear oscillations are still periodic but are better suited to be analyzed using the STFT and continuous wavelet analysis. The dominant frequency calculation is still possible as opposed to a power spectral density-based analysis. Within the finite simulation intervals considered here, the pairwise synchronization-error measures generally decrease from the dispersed initial conditions, indicating increasing similarity among the simulated neuronal trajectories. The present calculations do not establish asymptotic convergence for arbitrary initial conditions. However, this study did not investigate the synchronization performance of the oscillators under random perturbation conditions after the synchronization. This aspect has been left for future work since this will need a new synchronizing feedback controller design to ensure the damping of such external disturbances. This paper assumes that the neurons or Hodgkin–Huxley cells are connected in parallel and aligned, not staggered. However, in a realistic scenario, there can be much more complex topology of the connected neurons, which may be investigated in future as an extension of this work. In Figure 25, we show the comparison of the dominant frequency using the CWT and STFT. It is found that the CWT always yields a monotonically decreasing pattern when coupling strength increases, whereas less robust estimation is obtained in the STFT. This is because the STFT has many tuning parameters like point of FFT, signal length, and window. Therefore, the sharp changes are considered as noisy estimation for the STFT, showing that the CWT provides a smoother frequency trend for the present data, whereas the STFT estimates show greater variation. Simulating at the specific coupling strengths involves a huge number of simulations of the networks and processing their waveforms. Since we observe a stable monotonic pattern in the CWT, it is not necessary to add more datapoints in between since it adds no extra information regarding how the dominant frequency changes with an increase in coupling strength. Similar to Figure 25, we see a noisier estimation using the STFT in Figure 16, whereas the CWT estimation gives a smoother upward pattern of the dominant frequency when the input current is increased.

The present results should be interpreted within the limits of the numerical protocol. The simulations used identical neurons, and random initial membrane voltages, finite network sizes, and relatively short observation windows were selected. Independent initial-condition realizations, confidence intervals, network-size scaling, neuronal heterogeneity, stochastic perturbations, and sparse or structured connectivity were not examined. The persistence of the reported trends under these changes therefore remains to be established. In addition, the dominant-frequency estimates depend on the adopted STFT/CWT settings and should primarily be interpreted through their comparative trends rather than as exact universal frequencies. These limitations define the range over which the present results should be generalized.

The present network is an idealized dynamical-system model and should not be interpreted as a direct model of a specific neurological disorder or clinical brain-stimulation protocol. Disease-specific applications would require appropriate anatomical topology, neuronal heterogeneity, and validation against experimental or clinical data.

6. Conclusions

In this study, we numerically characterized a finite all-to-all network of identical Hodgkin–Huxley neurons coupled through normalized membrane-voltage differences. For the investigated initial conditions and finite simulation intervals, the sampled applied-current values produced resting convergence, a transient single-spike response, recurrent firing, and intervals of reduced coherence followed by more coordinated activity. Pairwise state-error measures showed convergence of the membrane-voltage and gating-variable

trajectories under the investigated coupling conditions, while the STFT and CWT provided complementary descriptions of their time-localized spectral content.

Across the sampled current values, the dominant spectral component generally increased with applied current. Increasing coupling strength produced stronger temporal coordination and, under the present finite-time analysis procedure, a modest decreasing trend in the estimated dominant spectral component. The latter is reported as a numerical observation rather than as a universal asymptotic property of diffusively coupled HH neurons.

The results therefore provide a joint state-space, synchronization-error, and time–frequency characterization of this idealized coupled HH network. Robustness to repeated initial conditions, network size, neuronal heterogeneity, noise, and sparse or structured connectivity remains an important subject for future work.

Author Contributions: S.D. (Sarbani Das)—Methodology, Software, Formal Analysis, Investigation, Writing—Original Draft, Visualization; S.D. (Saptarshi Das)—Conceptualization, Validation, Data Curation, Writing—Review and Editing, Project Administration, Funding Acquisition; K.M.—Resources, Writing—Review and Editing, Supervision, Funding Acquisition. All authors have read and agreed to the published version of the manuscript.

Funding: This research received no external funding.

Data Availability Statement: No new data were created or analyzed in this study. Data sharing is not applicable to this article.

Acknowledgments: For the purpose of open access, the author has applied a Creative Commons Attribution (CC BY) license to any author-accepted manuscript version arising from this submission.

Conflicts of Interest: The authors declare no conflicts of interest.

References

1. Mannion, C.; Taylor, J. Information processing by oscillating neurons. In *Coupled Oscillating Neurons*; Springer: Berlin/Heidelberg, Germany, 1992; pp. 98–114.
2. Singer, W. Synchronization of cortical activity and its putative role in information processing and learning. *Annu. Rev. Physiol.* **1993**, *55*, 349–374. [CrossRef]
3. Koch, C.; Segev, I. The role of single neurons in information processing. *Nat. Neurosci.* **2000**, *3*, 1171–1177. [CrossRef] [PubMed]
4. Fitzgerald, R. Phase Synchronization May Reveal Communication Pathways in Brain Activity. *Phys. Today* **1999**, *52*, 17–19. [CrossRef]
5. Lytton, W.W. Computer modelling of epilepsy. *Nat. Rev. Neurosci.* **2008**, *9*, 626–637. [CrossRef] [PubMed]
6. Jiruska, P.; De Curtis, M.; Jefferys, J.G.; Schevon, C.A.; Schiff, S.J.; Schindler, K. Synchronization and desynchronization in epilepsy: Controversies and hypotheses. *J. Physiol.* **2013**, *591*, 787–797. [CrossRef] [PubMed]
7. Hramov, A.E.; Kharchenko, A.A.; Makarov, V.V.; Khramova, M.V.; Koronovskii, A.A.; Pavlov, A.N.; Dana, S.K. Analysis of the characteristics of the synchronous clusters in the adaptive Kuramoto network and neural network of the epileptic brain. In *Proceedings of the Saratov Fall Meeting 2015: Third International Symposium on Optics and Biophotonics and Seventh Finnish-Russian Photonics and Laser Symposium (PALS)*; International Society for Optics and Photonics: London, UK, 2016; Volume 9917, p. 991725.
8. Beuter, A.; Modolo, J. Delayed and lasting effects of deep brain stimulation on locomotion in Parkinson's disease. *Chaos Interdiscip. J. Nonlinear Sci.* **2009**, *19*, 026114. [CrossRef] [PubMed]
9. Park, C.; Worth, R.M.; Rubchinsky, L.L. Fine temporal structure of beta oscillations synchronization in subthalamic nucleus in Parkinson's disease. *J. Neurophysiol.* **2010**, *103*, 2707–2716. [CrossRef] [PubMed]
10. Watanabe, T.; Rees, G. Age-associated changes in rich-club organisation in autistic and neurotypical human brains. *Sci. Rep.* **2015**, *5*, 16152. [CrossRef] [PubMed]
11. Rosjat, N.; Popovych, S.; Daun-Gruhn, S. A mathematical model of dysfunction of the thalamo-cortical loop in schizophrenia. *Theor. Biol. Med. Model.* **2014**, *11*, 45. [CrossRef] [PubMed]
12. Cociu, B.A.; Das, S.; Billeci, L.; Jamal, W.; Maharatna, K.; Calderoni, S.; Narzisi, A.; Muratori, F. Multimodal functional and structural brain connectivity analysis in autism: A preliminary integrated approach with EEG, fMRI, and DTI. *IEEE Trans. Cogn. Dev. Syst.* **2017**, *10*, 213–226. [CrossRef]

13. Popovych, O.V.; Tass, P.A. Control of abnormal synchronization in neurological disorders. *Front. Neurol.* **2014**, *5*, 268. [CrossRef] [PubMed]
14. Gerstner, W. Time structure of the activity in neural network models. *Phys. Rev. E* **1995**, *51*, 738. [CrossRef] [PubMed]
15. Bressloff, P.; Coombes, S. Desynchronization, mode locking, and bursting in strongly coupled integrate-and-fire oscillators. *Phys. Rev. Lett.* **1998**, *81*, 2168. [CrossRef]
16. Morris, C.; Lecar, H. Voltage oscillations in the barnacle giant muscle fiber. *Biophys. J.* **1981**, *35*, 193–213. [CrossRef] [PubMed]
17. Izhikevich, E.M. Which model to use for cortical spiking neurons? *IEEE Trans. Neural Netw.* **2004**, *15*, 1063–1070. [CrossRef] [PubMed]
18. Prado, T.d.L.; Lopes, S.; Batista, C.; Kurths, J.; Viana, R. Synchronization of bursting Hodgkin-Huxley-type neurons in clustered networks. *Phys. Rev. E* **2014**, *90*, 032818. [CrossRef] [PubMed]
19. Hodgkin, A.L.; Huxley, A.F. A quantitative description of membrane current and its application to conduction and excitation in nerve. *J. Physiol.* **1952**, *117*, 500–544. [CrossRef] [PubMed]
20. Hansel, D.; Mato, G.; Meunier, C. Phase dynamics for weakly coupled Hodgkin-Huxley neurons. *Europhys. Lett.* **1993**, *23*, 367. [CrossRef]
21. Hansel, D.; Mato, G.; Meunier, C. Clustering and slow switching in globally coupled phase oscillators. *Phys. Rev. E* **1993**, *48*, 3470. [CrossRef] [PubMed]
22. Van Vreeswijk, C.; Abbott, L.; Ermentrout, G.B. When inhibition not excitation synchronizes neural firing. *J. Comput. Neurosci.* **1994**, *1*, 313–321. [CrossRef] [PubMed]
23. Zlotnik, A.; Li, J.S. Optimal entrainment of neural oscillator ensembles. *J. Neural Eng.* **2012**, *9*, 046015. [CrossRef] [PubMed]
24. Kurrer, C.; Schulten, K. Noise-induced synchronous neuronal oscillations. *Phys. Rev. E* **1995**, *51*, 6213. [CrossRef] [PubMed]
25. Zhou, C.; Kurths, J. Noise-induced synchronization and coherence resonance of a Hodgkin–Huxley model of thermally sensitive neurons. *Chaos Interdiscip. J. Nonlinear Sci.* **2003**, *13*, 401–409. [CrossRef] [PubMed]
26. Casado, J.M. Synchronization of two Hodgkin–Huxley neurons due to internal noise. *Phys. Lett. A* **2003**, *310*, 400–406. [CrossRef]
27. Ernst, U.; Pawelzik, K.; Geisel, T. Synchronization induced by temporal delays in pulse-coupled oscillators. *Phys. Rev. Lett.* **1995**, *74*, 1570. [CrossRef] [PubMed]
28. Ernst, U.; Pawelzik, K.; Geisel, T. Delay-induced multistable synchronization of biological oscillators. *Phys. Rev. E* **1998**, *57*, 2150. [CrossRef]
29. Batista, C.; Viana, R.; Lopes, S.; Batista, A. Dynamic range in small-world networks of Hodgkin–Huxley neurons with chemical synapses. *Phys. A Stat. Mech. Its Appl.* **2014**, *410*, 628–640. [CrossRef]
30. Ozer, M.; Perc, M.; Uzuntarla, M. Stochastic resonance on Newman–Watts networks of Hodgkin–Huxley neurons with local periodic driving. *Phys. Lett. A* **2009**, *373*, 964–968. [CrossRef]
31. Nabi, A.; Moehlis, J. Single input optimal control for globally coupled neuron networks. *J. Neural Eng.* **2011**, *8*, 065008. [CrossRef] [PubMed]
32. Breakspear, M.; Heitmann, S.; Daffertshofer, A. Generative models of cortical oscillations: Neurobiological implications of the Kuramoto model. *Front. Hum. Neurosci.* **2010**, *4*, 190. [CrossRef] [PubMed]
33. Pan, I.; Das, S.; Routh, A. Towards a global controller design for guaranteed synchronization of switched chaotic systems. *Appl. Math. Model.* **2015**, *39*, 2311–2331. [CrossRef]
34. Sejdic, E.; Djurovic, I.; Stankovic, L. Quantitative performance analysis of scalogram as instantaneous frequency estimator. *IEEE Trans. Signal Process.* **2008**, *56*, 3837–3845. [CrossRef]
35. Golomb, D.; Rinzel, J. Dynamics of globally coupled inhibitory neurons with heterogeneity. *Phys. Rev. E* **1993**, *48*, 4810. [CrossRef] [PubMed]
36. Golomb, D.; Wang, X.J.; Rinzel, J. Synchronization properties of spindle oscillations in a thalamic reticular nucleus model. *J. Neurophysiol.* **1994**, *72*, 1109–1126. [CrossRef] [PubMed]
37. Wang, X.J.; Buzsáki, G. Gamma oscillation by synaptic inhibition in a hippocampal interneuronal network model. *J. Neurosci.* **1996**, *16*, 6402–6413. [CrossRef] [PubMed]
38. Traub, R.D.; Kopell, N.; Bibbig, A.; Buhl, E.H.; LeBeau, F.E.; Whittington, M.A. Gap junctions between interneuron dendrites can enhance synchrony of gamma oscillations in distributed networks. *J. Neurosci.* **2001**, *21*, 9478–9486. [CrossRef] [PubMed]
39. Olhede, S.C.; Walden, A.T. Generalized morse wavelets. *IEEE Trans. Signal Process.* **2002**, *50*, 2661–2670. [CrossRef]
40. Han, S.K.; Kurrer, C.; Kuramoto, Y. Dephasing and bursting in coupled neural oscillators. *Phys. Rev. Lett.* **1995**, *75*, 3190. [CrossRef] [PubMed]
41. Tinkhauser, G.; Pogosyan, A.; Little, S.; Beudel, M.; Herz, D.M.; Tan, H.; Brown, P. The modulatory effect of adaptive deep brain stimulation on beta bursts in Parkinson's disease. *Brain* **2017**, *140*, 1053–1067. [CrossRef] [PubMed]

42. Izhikevich, E.M. Simple model of spiking neurons. *IEEE Trans. Neural Netw.* **2003**, *14*, 1569–1572. [CrossRef] [PubMed]
43. Szatmáry, B.; Izhikevich, E.M. Spike-timing theory of working memory. *PLoS Comput. Biol.* **2010**, *6*, e1000879. [CrossRef] [PubMed]

Disclaimer/Publisher's Note: The statements, opinions and data contained in all publications are solely those of the individual author(s) and contributor(s) and not of MDPI and/or the editor(s). MDPI and/or the editor(s) disclaim responsibility for any injury to people or property resulting from any ideas, methods, instructions or products referred to in the content.